A Science Instrument Concept Study Report

A High-Efficiency, Wide-Band, Multi-Object, Near-Infrared Spectrograph for the NGST

Principal Investigator

Dr. S. Harvey Moseley
Code 685
Goddard Space Flight Center
Greenbelt, MD 20771
301-286-2347
301-286-1617 (FAX)
moseley@stars.gsfc.nasa.gov

Co-Investigators

Dr. Bruce E. Woodgate, GSFC
Dr. Randy A. Kimble, GSFC
Dr. Charles W. Bowers, GSFC
Dr. Alexander S. Kutyrev,GSFC/Raytheon ITSS
Dr. Rainer K. Fettig, GSFC/Raytheon ITSS
Dr. Jonathan P. Gardner, GSFC
Dr. Harry I. Teplitz, GSFC/NOAO
Dr. Eliot M. Malumuth, GSFC/Raytheon ITSS
Dr. Johnathan L. Kuhn, GSFC
Richard P. Wesenberg, GSFC
J. Eric Mentzell, GSFC

Contents

1 Science **1**

1.1 Executive Summary . . . 1
1.2 Introduction . . . 2
1.3 NGST Spectrograph Requirements . . . 3
1.3.1 Counts And Sizes Of Galaxies. . . . 4
1.3.2 Spectrograph Operations . . . 4
1.3.3 Simultaneous Observations . . . 6
1.3.4 Serendipity Modes . . . 8
1.3.5 Target Selection For Spectroscopy . . . 11
1.4 MOS Operational Modes . . . 12
1.4.1 Resolutions And Fields Of View Of The Imager And Spectrometer . . . 12
1.4.2 Low Resolution–Prism Mode . . . 12
1.4.3 Low Resolution Prism Assembly . . . 13
1.4.4 Moderate Resolution(s) Mode . . . 14
First Order Gratings Method . . . 14
Echelle With FTS Order Sorter Method. . . . 15
1.4.5 Sensitivity Estimates For Different Modes. . . . 16
1.4.6 Dithering And Readout Noise. . . . 17
1.4.7 Optical Requirements For A Field Selector . . . 18
Pixel Size . . . 19
Cryogenic Operation . . . 20
Fill Factor . . . 21
Other Requirements . . . 21

2 Engineering: Development Of Microshutters **23**

2.1 Overview . . . 23
2.2 Background . . . 24
2.3 Microshutter Concept . . . 25
2.3.1 Torsion Beam Suspension . . . 25
2.3.2 Actuation . . . 26

2.3.3 Selection Electronics . . . 26
2.4 Development Process With Rapid Prototyping . . . 28
2.4.1 Manufacturing And Test Facilities . . . 29
2.4.2 Mechanical Analysis And Material Properties . . . 29
Material Stiffness . . . 30
Material Strength . . . 32
Single Shutter Tests . . . 33
Mechanical Summary . . . 34
2.4.3 Single Shutter Actuation . . . 35
2.4.4 Actuation Schemes And Shutter Arrays . . . 35
2.5 Transition To Production Technology . . . 35
2.6 Technology Readiness . . . 37
2.6.1 Current Status . . . 37
2.6.2 Development Plan . . . 38
2.6.3 Readiness By Instrument Selection . . . 40
2.7 Development Schedule and I & T . . . 40
2.7.1 Microshutter Development Schedule . . . 40
Microshutter Specific I & T Issues . . . 40

3 Cost Estimate 45
3.1 Cost Summary . . . 45
3.2 Details . . . 45
3.2.1 Management . . . 45
3.2.2 Science Program Development . . . 45
3.2.3 Systems Engineering . . . 46
3.2.4 SR&QA . . . 46
3.2.5 Structure . . . 46
3.2.6 Optics . . . 46
3.2.7 Electronics . . . 47
3.2.8 Thermal Engineering . . . 47
3.2.9 Software . . . 47
3.2.10 Detectors . . . 47

A A Comparison of the Prism Mode with Multi-Filter Imaging 48
A.1 Motivation . . . 48
A.2 Photometric Redshifts . . . 48
A.3 Simulations . . . 49
A.4 Optimal Resolutions . . . 50
A.5 Advantage of a Prism . . . 51
A.6 Conclusions . . . 52

Bibliography **58**

List of Figures

1.1 Sizes of Galaxies in the HDF-S 5
1.2 Comparison of prism mode to multiple filters 6
1.3 Accuracy of redshifts with the prism mode and multiple filters 7
1.4 Sensitivity to Emission Line Galaxies 9
1.5 Photometric redshifts in the HDF-N 11
1.6 Prism mode resolution 14
1.7 Minimum detectable flux in the spectrograph 17
1.8 Instrument layout of first order grating/prism MOS 19
1.9 Instrument layout of echelle/FTS/prism MOS 20
1.10 The MOS Design Integrated with the NGST 21

2.1 Schematic and scanning electron micrograph of the basic shutter design 26
2.2 SEM image of a single shutter blade in various positions 27
2.3 3D doubleshutter actuation sequence 28
2.4 a) Schematic drawing of the cantilever beam vibration test specimen. b) Scanning electron micro-graph of machined cantilever beam. 30
2.5 Scanning Electron Migrographs of a silicon "T" beam with dimensions of $L_a = 6.55\ \mu m$, $w_a = 6.25\ \mu m$, $L_b = 60\ \mu m$, $w_b = 30\ \mu m$, and thickness $t = 1.9\ \mu m$. a) SEM of "T" beam bending prior to failure. b) Fracture surface after failure. 33
2.6 180°rotation of the shutter blade. 34
2.7 Layout of the 2048 by 2048 microshutter array. 512 by 512 shutter arrays are arranged in mosaic on a frame with 2 mm thick ribs. Expanded views shows the corner of the mosaic and single microshutter. 36
2.8 Development schedule for the transmissive microshutter array component. Tasks are identified in section 2.6.2. 41
2.9 Flight qualification of a transmissive microshutter array for an MOS instrument. All testing will be performed at cryogenic temperatures. 42

3.1 Estimated cost to develop a transmissive microshutter array for a MOS instrument. 46

A.1 The redshift distribution of galaxies in our simulation 50
A.2 The number-magnitude of simulated galaxies 51

A.3 The resolution as a function of wavelength for the prism 52
A.4 Recovered redshifts compared to input redshifts as a function of resolution 53
A.5 Recovered input redshifts as a function of redshift 54
A.6 The fraction of recovered redshifts 55
A.7 Percentage of recovered redshifts–faint galaxies 56
A.8 Percentage of recovered redshifts–faintest galaxies 57

List of Tables

1.1 Emission Lines in MS1512−cB58 10
1.2 Grating Characteristics 15
1.3 MOS microshutter array requirements 22

2.1 Funds available for transmissive microshutter development as of September 1999. . 37
2.2 Estimated TRL level for a microshutter based MOS as of now 43
2.3 Projected TRL for a microshutter based MOS at instrument selection 44

A.1 Efficiency and background assumptions 49

Chapter 1

Science

1.1 Executive Summary

We report on our study of innovative concepts for a high-efficiency, wide-band, multi-object near-infrared spectrograph for the NGST. The spectrograph will simultaneously cover the wavelength range of 0.6-5 μm with a 4K $\times$ 4K mosaic array of InSb detectors and will offer low resolution spectroscopy (R $\sim$ 25-100) of thousands of objects simultaneously, higher resolution spectroscopy (R $\sim$ 1500-5000) of more than a thousand objects simultaneously, and an imaging mode for initial target acquisition and configuration of a high transmission entrance aperture mask.

The entrance aperture mask, a programmable microshutter array, has been successfully developed to the level of a 3$\times$3 array, demonstrating the basic mechanical and electrostatic cell operation. It is ready to be scaled up to larger arrays in the next development phase.

Our spectrograph conceptual design includes two principal features to address the demanding scientific requirements of the NGST, whose primary targets will typically be highly redshifted and extremely faint:

- Our lowest resolution spectrograph design is based on refractive dispersing elements (prisms) that permit us to obtain spectra over the entire near-IR range of 0.6-5 μm ($>$3 octaves) simultaneously for all objects observed, rather than the $<$1 octave of coverage (to avoid order confusion) available with a typical grating spectrograph. The use of prisms as the only transmissive or dispersing elements, provides both substantially higher throughput than grating/order sorter combinations as well as the significant multiplexing advantage of complete wavelength coverage in one exposure.

- For higher resolutions than those available to prisms, we evaluate the trade-off between using 3 or more first order gratings for each required resolving power to cover the 0.6-5 μm range, and covering this range in a single exposure by using low order echelles cross-dispersed by an imaging Fourier transform spectrograph.

While the first two modes require (and reap the benefits of) target selection, our design can also be operated in serendipity mode. In this mode, slits up to $3''$ wide can be opened on blank sky in each row to search for pure line emission galaxies at high redshift. The ultra-wide slit returns the sensitivity to narrow emission lines of the R=1500 mode, with a minimum accuracy of 0.01 in the redshift determination, over a 1140 square arcsecond field of view.

This combination of a high efficiency spectrograph with a high efficiency programmable entrance mask will provide a powerful near-IR spectroscopic capability for the NGST.

This report describes the first design for a programmable transmission mask for a MOS. In our study, we have:

- developed the concept for the microshutter array, including individual shutter operation and the selection and actuation mechanism for essentially random access addressing
- measured strength and stiffness of candidate materials for shutters, selected materials for fabrication, and optimized their mechanical design
- tested the mechanical properties of individual shutters, and built and actuated small microshutter arrays
- developed plans for the production of larger arrays to be fabricated with integrated shutter selection electronics using photolithographic processes

Pursuing this development program aggressively, we can demonstrate technical readiness with a full scale microshutter array by the Apr. 2001 NGST instrument selection.

1.2 Introduction

Efficient, low- to moderate-resolution spectroscopy in the near infrared is at the heart of NGST's scientific goals [1]. For the highly redshifted objects that will reveal the origins of galaxies, clusters, and large scale structures in the universe, spectroscopic coverage of the 0.6-5 μm band will provide vital information. For galaxies observed at the peak of the merging and star forming era (z $\sim$ 1-3), rest-frame visible light from their older stellar populations will be seen in the near IR. For the earliest star forming galaxies (at z = 5-10 or more), even the rest-frame far-ultraviolet output of newly formed stars and the spectral signatures of the earliest observable supernovae will be redshifted to these wavelengths.

Low-resolution spectroscopy (R $\sim$ 25-100) will be crucial for obtaining spectral energy distributions (SEDs) of distant galaxies. The SEDs will be used for determining redshifts by the observation of spectral breaks or edges (e.g. the 1.6μm bump, the 4000Å break, or even the Lyman limit for very high z), and for measuring the amount of star formation in the earliest galaxies from the spectrum of their redshifted UV light. This resolution is also well matched to the detection of broad (few thousand km/sec) emission lines of distant quasars and for spectral confirmation of

distant supernovae. For all of these tasks, simultaneous observation of many objects in a single field will be crucial for efficiently compiling statistical samples and discovering rare objects.

What is the optimum resolving power for obtaining spectra of the faintest sources? Very rough redshift indications will be available from broadband imaging by fitting galaxy models with spectral slopes and breaks to the photometry. In principle this could be continued to higher resolving powers by using more and narrower filters to obtain more accurate redshifts, but this would require further sub-dividing the observing time. We have run Monte Carlo simulations of this method to find the accuracy of redshift determination as a function of the number of filters, and then compared the sensitivity of using the optimal number of filters with a single spectral observation using a prism with the same resolving power. These simulations are discussed in Appendix A, which concludes:

Low resolution prism observations of galaxy SED's provide a significant advantage over multi-filter observations for any realistic observing strategy. For an ideal prism in background limited observing, the prism has a signal-to-noise advantage of square root of the resolution over serial observations by filters with similar resolution. This added depth reaches at least a magnitude fainter in recovery of photometric redshifts with the prism over filter observations at *any* resolving power. Extensive simulations suggest that in 10^5 seconds an ideal prism will recover the redshift of 80% of measured objects (subject to MOS selection) down to $K_{AB} = 32$, with an accuracy of $\delta_z < 3\%$, compared to less than 40% of the objects with serial filter observations.

A field would be imaged with the camera, (or alternatively with the spectrograph in its imaging mode,) and candidates would be selected for observation through the microshutter array with a prism for accurate redshift determination. The selection of targets could be done on the basis of magnitude and position alone, or could make use of colors and photometric redshifts when available.

Higher resolution (R $\sim$ 1500) spectroscopy is suitable for measuring the velocity dispersions of distant clusters and merger components. This resolution (a few hundred km/sec) is also well matched to the detection of narrow emission lines from star forming galaxies and AGN (and determining redshifts from them). The measurement of velocity dispersions of clusters of galaxies allows an estimate of the masses of the clusters, including the dark matter. Knowledge of the ratio of light-emitting to dark matter as a function of redshift is crucial to constrain theories of large scale structure formation.

We describe below a concept for a highly efficient, wide-band, multi-object near-IR spectrograph to enable NGST to carry out these critical scientific goals.

1.3 NGST Spectrograph Requirements

In this section we discuss the requirements for a NIR spectrograph designed to satisfy the scientific goals of NGST. We wish to obtain spectra to investigate the very faintest galaxies observable, with the greatest possible multiplexing advantage.

1.3.1 Counts And Sizes Of Galaxies.

A primary goal of NGST is to investigate the earliest galaxies, beyond redshift 5, to detect them and measure their redshifts, determine physical conditions, and elemental abundances. Efficient use of the NGST facility on these very faint sources requires the most sensitive spectrograph possible. The field of view and number of input apertures should be chosen to provide efficient observation given the observed number counts of candidate objects for spectroscopic study.

Long exposures with NGST are expected to reach magnitudes AB=34 for imaging and AB=26 to 32 for spectroscopy, depending on the resolving power and spectral character of the galaxies. The best currently existing measurements of faint galaxy counts is from the HST observations of the Hubble Deep Field North and South [2, 3, 4, 5]. The faintest galaxies yet observed are those in the STIS CCD image of the HDF-S, at AB>30. In this field, the number density of galaxies brighter than AB=30 is 3×10^6 objects degree^{-2}, or 7500 objects in the 3'×3' field of view of the baseline ISIM spectrograph design [6]. While these measurements were made in visible light, by fitting models to the STIS and NICMOS observations in the HDF-S [7], galaxy counts can be estimated for the NIR, reaching 3.5×10^6 at 1 nJy ($K_{AB} = 31.4$).

The faintest galaxies are barely resolved at the STIS resolution, with a median half-light radius of 0.1 arcsec (see Figure 1.1). Comparing the observed sizes of the STIS and NICMOS images, and then correcting for the NICMOS resolution, it is estimated that the sizes in the NIR would be slightly smaller than in the visible, as the bulges of the galaxies become more prominent at longer wavelengths. Galaxies at the isophotal detection limit of the HDF-S STIS image occupy only ∼5% of the image, well below the confusion limit.

1.3.2 Spectrograph Operations

Given the known dilute filling factor for galaxies bright enough for NGST spectroscopy, is it necessary and efficient to obtain spectra for every pixel of each field? Methods which do not require an entrance aperture mask must observe every pixel in their fields. The sensitivity of Fourier Transform Spectrometers for obtaining the spectrum of each object is limited by the broad-band sky background illuminating each pixel. With a reasonable number of detectors, Integral Field Spectrographs can be built to fill less than 0.02 - 0.1 of the baseline NGST spectrograph field, and so would need 10 - 50 observations to cover this area. A Multi-Object Spectrograph (MOS) can be built with optimal sensitivity for each object, and cover more than the NGST baseline field.

Targets for a MOS will need to be selected from among those observed with an imager, since for long exposure times, ($\geq 10^5$ sec,) there are more objects in the field than MOS apertures that can be opened without spectral overlap.

The number of objects simultaneously observable with a MOS depends on the detector space required for each spectrum, the field size and the aperture size of each slit in the MOS. For this discussion we assume an individual aperture size of 0.100 mm, subtending 0.093 arcsec at the focal plane. A 2K×4K array of these apertures will cover a field of 3.2×6.3 arcmin, 2.2 times

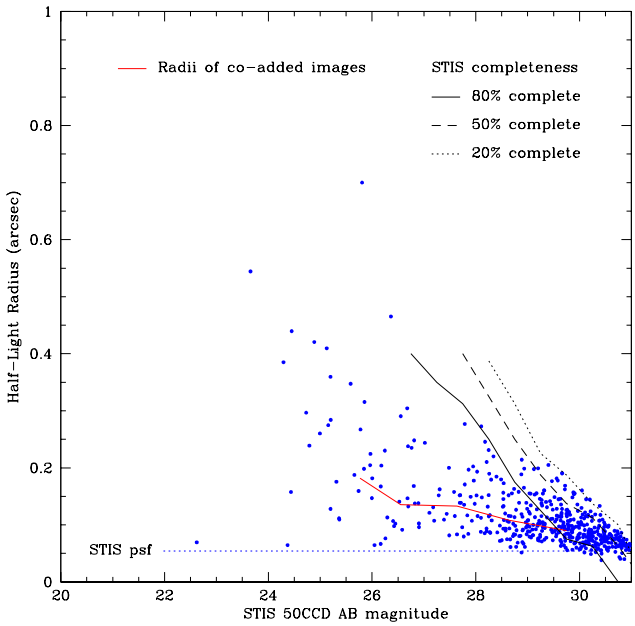

Figure 1.1: Sizes of galaxies in the HDF-S STIS 50CCD image, from [6]. The half light radii of the objects are plotted as a function of AB magnitude. Also shown are the half-light radius of the point spread function, and the results of Monte Carlo simulations run to determine selection effects. At AB$<$29, the median half-light radius approaches 0.1 arcsec, and the distribution is significantly smaller than the completeness limits. While selection effects are operating on the measured sizes and completeness of HDF-S catalog at the faintest levels, it is clear that the tendency of fainter galaxies to be more compact is a real effect.

the nominal NGST baseline spectroscopy field area. (We suggest demagnifying this field onto a 4K$\times$4K detector, using an optical magnification of 0.27. A detector pixel size of 0.027 mm would project to 0.093 arcsec on the sky. The extra 2K pixels in the dispersion direction allows recording of full spectra for all field points at R=1500, while conserving area within the focal plane.) While the slitsize and the detector pixel size are the same, exact alignment of the two would be difficult. Then for objects centered on a slit in the spatial direction, we allocate one slit and 2 detector pixel rows. For objects centered between 2 slits, we allocate two slits in the spatial direction, and 3 detector pixel rows. Since the objects will be randomly distributed on the sky, each galaxy will occupy 2.5 pixel rows, on average.

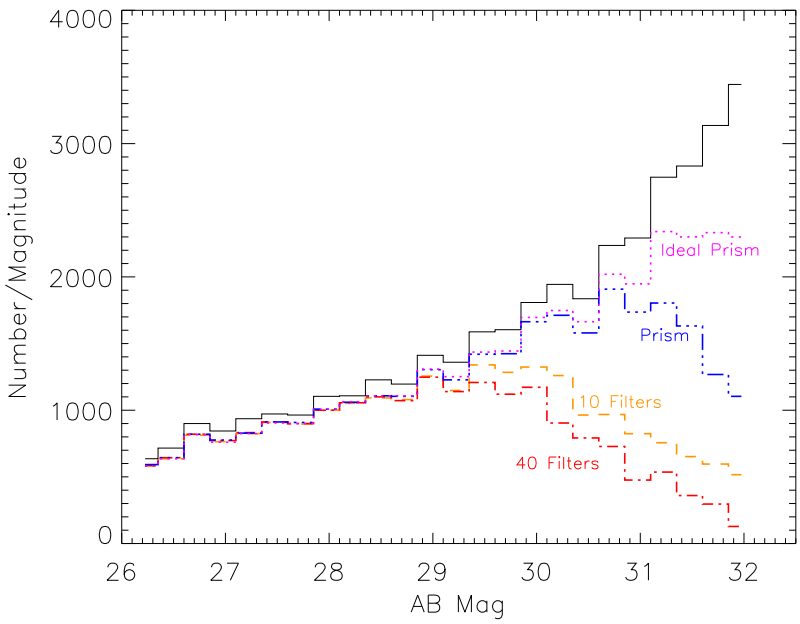

Figure 1.2: A comparison of the prism mode to photometric redshifts from multiple filter observations. Because the prism mode obtains full wavelength coverage for the entire exposure time, it is able to obtain accurate redshifts for fainter objects than imaging through moderate resolution filters.

1.3.3 Simultaneous Observations

For R=1500, with a spectral length of 2000 pixels, one spectrum from any field point can be fitted along the dispersion direction. With 4096 pixels in the cross-dispersion direction, and using 2.5 spatial pixels per object, up to 1600 objects can be selected.

In the prism mode, at R$\sim$40, the spectral length is $\sim$300 pixels, and up to 6 spectra can be fitted along the dispersion direction. In the cross-dispersion direction, up to 1600 objects can be selected, providing up to 10,000 spectra over the field. Simulations show that given randomly positioned galaxies, and the same number of slits as galaxies, approximately 60% of the slits could be utilized. This is a minimum; the efficiency goes up when there are more galaxies than slits, or when there are more slits than galaxies. When there are three times as many galaxies as slits, the slit use efficiency is above 95%.

The number of candidate objects available for detection in a given observing time for spectroscopy will depend on the area the MOS can cover, the spectral resolving power used, and whether continua or emission lines are to be sought.

For the R$\sim$40 prism mode described below, a continuum source of 4nJy can be detected at 10

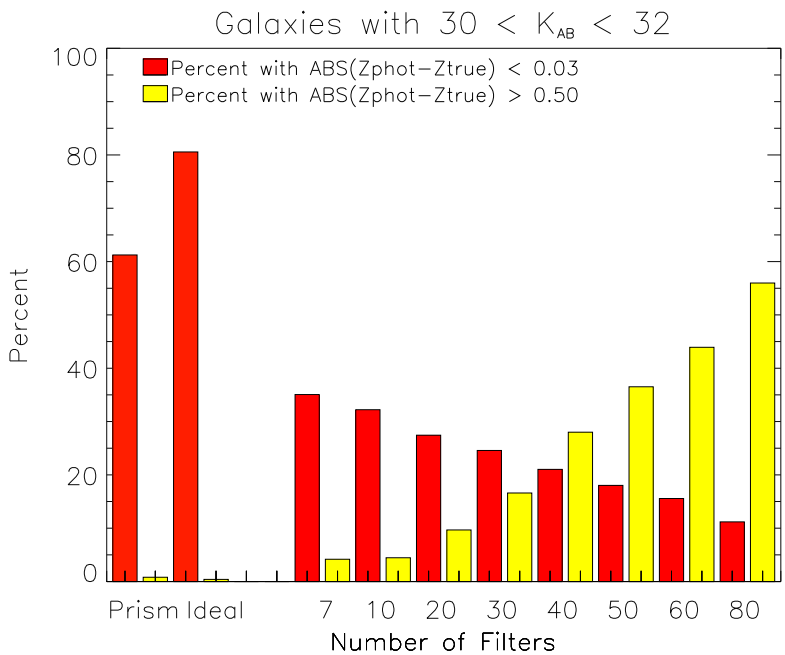

Figure 1.3: A comparison of the prism mode to photometric redshifts from multiple filter observations. For galaxies with 30< K_{AB} <32, the prism mode obtains accurate redshifts ($\Delta_z < 0.03$) for 60% of the targetted galaxies, while getting the redshifts badly wrong only a few percent of the time. An ideal prism, with constant resolution accross the wavelength range, does even better. In comparison, the same amount of exposure time spent with filter imaging does substantially worse, both in the number of redshifts it determines with high accuracy, and in the number of catastrophic failures.

σ per resolution element in 10^5 sec[1]. This corresponds to magnitude AB=29.9. Simulations have shown that the prism mode could determine redshifts substantially fainter than this, recovering ∼60% to 80% of the galaxies at 30< K_{AB} <32, as shown in Figures 1.2 and 1.3. The simulations are discussed in Appendix A. In a 3.2×6.3 arcminute field of view, there are 24,000 galaxies with K_{AB} <32 so with ∼6000 apertures we need to down select by a factor 4. Similarly, the MOS could observe nearly all the objects down to this magnitude without further selection in 4 to 5 exposures. In contrast, an IFS with 30×30 arcsec field of view, would take over 100 exposures to cover the same field. The advantage of the MOS over the IFS is that objects can be selected by their photometric properties, and thus it is not necessary to take 4 to 5 exposures per field.

[1]In our simulations and calculations we assume a total exposure time of 10^5 seconds, or 28 hours. The longest exposures making up an "NGST deep field" could be 10^6 seconds or more. Most of our calculations scale simply as $\sqrt{t}$. Rather than considering one or two of the deepest observations that NGST will make, which would probably be optimized differently from the norm, we have chosen to consider typical deep exposures

Figure 1.2 shows that the prism mode gives its greatest advantage over broadband photometric redshifts in the faintest two magnitude bins. With prior selection on the basis of magnitude alone, the prism mode could observe the spectral energy distribution of every object in the field of view with $30.2 < K_{AB} < 32.0$, losing only the $< 40\%$ of the objects for which the spectra would overlap. Likewise, if photometric redshifts were available from broadband imaging, the prism could observe all of the $z > 1.6$ objects with $>60\%$ selection efficiency. *Faint, high-z galaxies are the prime discovery space for NGST.*

For the R=1500 mode, a continuum source of 300 nJy can be detected at 10σ per resolution element in 10^5 sec, corresponding to magnitude AB=25.2. The number of objects to select from in the above field is $\sim$2100, so with 1600 apertures we would need to down select by a factor 1.3 which would come simply from the need to avoid overlapping spectra. Again, all the objects could be observed in 2 exposures, compared to over 100 for an IFS. However, there may be many objects of interest with fainter continua, for which it would be possible to detect emission lines.

A NIR spectrum of the gravitationally lensed z=2.72 galaxy MS1512−cB58 was obtained recently using NIRSPEC on Keck [8]. The object is typical of Lyman Break Galaxies at z$>$ 2.5 [9]. Using the equivalent widths of this galaxy, given in Table 1.1, we have calculated the continuum magnitude of galaxies for which we could detect the lines. We plot these magnitude limits as a function of redshift in Figure 1.4. We would be able to detect two or more lines at the 5σ level for galaxies fainter than AB=29.0 over nearly the whole redshift range 0.5$<$z$<$9.0, and a single line ([O II]) out to z=12.5. This galaxy does not show Lyα in emission, so it has not been included. However, we also plot in this figure what would be the measured broad-band AB magnitude (in a 25% bandpass filter) of a pure Lyα emission line source with no continuum, detected at the 5σ sensitivity of our R=1500 spectrograph.

At $K_{AB} < 29$, there are 9300 galaxies in the field of view. With 1600 slits, we would need to down-select by a factor of 6. The selection could be done by one of several ways. A pure magnitude selection would allow simultaneous spectra of 60% of the objects with 28$<$ K_{AB} $<$29. Alternatively, the prism mode could be used to determine photometric redshifts, and all of the galaxies at z$>$2 could be targeted, subject to the 60% filling factor of the slit geometry.

If instrument packaging allows, higher resolving power spectroscopy could be included for more detailed spectroscopic studies using both emission and absorption lines. For R$\sim$5000, rotations and kinematics of galaxies, elemental abundances, and gas dyamics may be studied. Full spectra can be obtained for 40% of the field area. A continuum source with AB=23.1 can be detected at 10 sigma per spatial and spectral resolution element in 10^5 sec. If we assume that each object occupies 0.4” in the spatial direction, this mode could observe 950 objects simultaneously, targetting all of the $\sim$600 galaxies in the field with $K_{AB} < 23.1$.

1.3.4 Serendipity Modes

The modes described above require pre-selection of objects from prior imaging information. An IFS or FTS, which looks at every pixel within their fields, are able to serendipitously identify

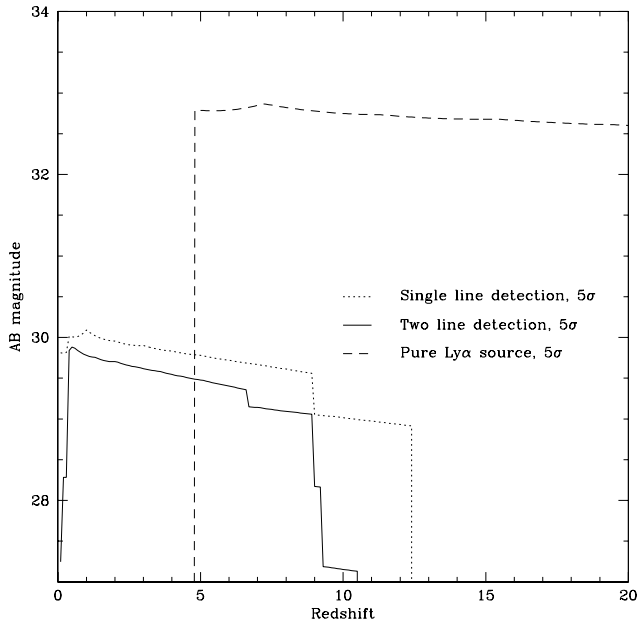

Figure 1.4: The sensitivity of the R=1500 mode to emission line galaxies. Using the z=2.72 galaxy MS1512−cB58 as a template, we plot the continuum AB magnitude as a function of redshift, if it were placed at our 5σ line detection limit. We would be able to detect a single line from an AB>29.0 galaxy over the full redshift range z<12.5, and two or more lines over the redshift range 0.5<z<9.0. We also plot the measured broadband magnitude of a pure Lyα emission line source at the 5σ line detection limit.

emission line galaxies or AGN which are too faint to appear in deep images. Our MOS would also be able to search for such objects by opening a wide slit in each row on a part of the sky which is devoid of objects. By opening a 3 arcsecond wide slit, with the R=1500 grating, the resolution in redshift of the MOS would be degraded to R=100 for a single line source. In this case it would not be possible to know where within the 3 arcsecond slit the galaxy lies, and an additional observation at a different roll angle would be required to identify the source. However, since the wavelength zero point will be known to an accuracy of $\Delta\lambda/\lambda = 0.01$, if two or more lines are detected and identified, then the zero-point position and exact redshift can be deduced from the ratio of the observed wavelengths of the two lines.

The MOS could also be operated in parallel mode with no imaging pre-selection, while the imaging camera is conducting other observations. A 3 arcsecond-wide slit with the R=1500 grating could be opened for the whole (spatial) length of the spectrograph. Most of the time would be spent with the grating in place, but a short imaging exposure with all of the slits open would be taken to establish the wavelength zero-point for each object. The sensitivity in this case would be

Line	λ_{obs}	z_{em}	W_0^a	F^b
[O II] λ3726/3728	1.1.3898	2.72897	37±5	17.48±0.26
Hγ λ4340	1.61828	2.72875	9±1	1.61±0.17
Hβ λ4861	1.81217	2.72774	26±4	4.07±0.57
[O III] λ4959^c	1.84913	2.72890	26±8	4.01±1.30
[O III] λ5007	1.86678	2.72845	97±5	14.73±0.78
He I λ5876	2.19100	2.72873	3±1	0.35±0.09
[OI] λ6300	2.34949	2.72935	25±4	3.06±0.46
[N II] λ6548	2.44204	2.72944	7±2	0.86±0.21
Hα λ6563	2.44750	2.72935	106±3	12.56±0.37
[N II] λ6583	2.45566	2.73031	10±2	1.14±0.26

Table 1.1: Measurements of emission lines in the gravitationally lensed z=2.72 galaxy MS1512−cB58 obtained using NIRSPEC on Keck [8]. We use these equivalent widths to determine the sensitivity of our R=1500 mode to emission line galaxies at $0 < z < 12.5$. NOTES: ^{a}Rest-frame equivalent width in Å. ^{b}Observed line flux in units of 10^{-16}ergs s^{-1} cm^2. ^{c}The blue wing of the 4959Å line is in a deep atmospheric absorption trough.

equivalent to an R=100 grating, i.e., still detector noise limited. In this "pseudo-slitless mode", a 1140 square arcsecond field of view would be observed, and a spectrum of resolving power R=1500, (degraded by the object's size for extended continuum sources,) would be obtained. The effective beam size for confusion in this case would be 2 slits in the spatial direction and 30 slits in the spectral direction, or 0.6 square arcseconds. At $K_{AB} < 25.2$ there is about one object in every 35 square arcseconds, so studies reaching that depth would not suffer from confusion. For the longest "NGST deep field" observations, imaging the spectroscopic parallel fields in advance would elimate confusion, allow selection of the likely high-redshift targets, and make for the most efficient use of the observatory. However, the "pseudo-slitless" method would allow the MOS to make use of the shorter parallel opportunities in a self-contained manner.

The MOS can duplicate the abilities and field of view of an IFS with the same number of detector pixels, in almost every respect. Spatially resolved spectroscopy of bright objects could be obtained by stepping a slit across a bright object at each read-out, while continuing to accumulation exposure time on fainter galaxies. In the "pseudo-slitless" mode, the size of the slit desired depends on the trade between sky noise, detector noise, field of view, and spectral resolution. With the MOS, this trade could be made after the noise characteristics have been measured on-orbit, and can be changed for different observations to reflect their scientific priorities. For an IFS, the trade between spectral resolution and field of view must be made in the design phase, well before launch.

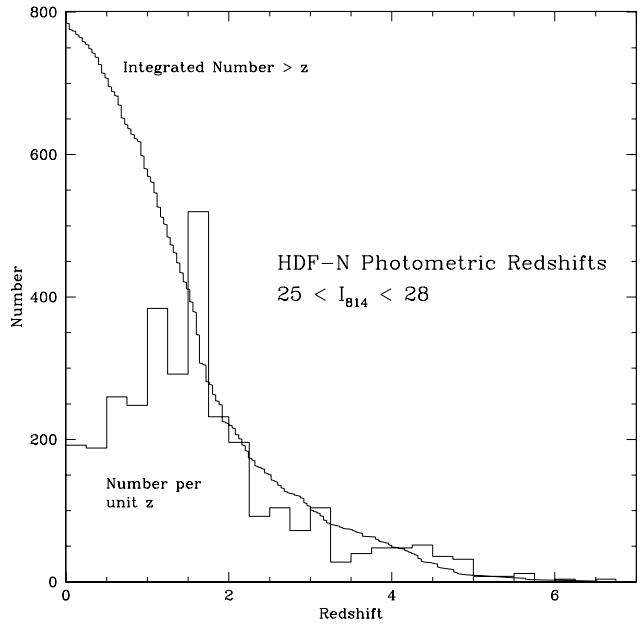

Figure 1.5: Photometric redshifts of galaxies with $25 < I_{814} < 28$ in the HDF-N, as determined by [10]. Both the differential histogram of the redshifts, and the integrated number greater than z are plotted. This figure shows that using photometric redshifts to pre-select objects with z>2 would reduce the number of targets by a factor of four.

1.3.5 Target Selection For Spectroscopy

Objects may be selected with a variety of criteria, depending on the scientific goals of the study:

Redshift distributions for faint galaxies are available for the Hubble Deep Field North, from photometric redshifts and from Keck spectroscopic confirmations [11, 12, 13]. The HDF-N results plotted in Figure 1.5 [10] show that for magnitudes between 25 and 28 selecting galaxies with z>2 on the basis of photometric redshifts from the imaging would reduce the number of targets by a factor of 4, which is more than we require.

Similarly, criteria from the imaging photometry could be chosen to pick out candidate AGN spectra, supernovae, or emission line galaxies. Some object classes objects may be rarer than the factor 4 down-selection ratio from the magnitude limited samples above, but candidates satisfying rare object criteria with emission line domination can be drawn from the larger samples of deeper imaging surveys down to AB=34.

Our spectrometer design allows simultaneous observations of all high-z candidates in a large field of view. *This is the best one can do*.

1.4 MOS Operational Modes

The MOS operational modes described below can be interchanged by supporting the prism assembly, the gratings, and a mirror on a wheel.

1.4.1 Resolutions And Fields Of View Of The Imager And Spectrometer

Considerations of observing strategy and minimizing development costs suggests that the fields of view and spatial resolutions of the imager and spectrograph should be considered together. Spectroscopic observations guided by prior imaging, as needed for locating apertures in a MOS, or for locating a smaller IFS aperture, suggest that the field of the spectrograph should be the same as or within the imager field, so that the prior observations for selection would be available.

The development of a detector mosaic, for example a 4K$\times$4K array, out of smaller detector chips, is very expensive. It is likely to be cost effective for the spectrograph to use the same array size as the imager, rather than develop a different mosaic, even when made out of the same detector chip size.

The optimal detector pixel size on the sky may be quite different between the imager and the spectrograph. For the imager, obtaining the full spatial resolution available from the 8-meter telescope is an important goal for measuring the sizes and structure of galaxies and detecting them above the zodiacal background, whereas the detector noise background should be small for R$\lesssim$ 20. This leads to a pixel size between 0.025 and 0.05 arcsec. For the spectrograph, the detector dark and read noise will be dominant over zodiacal background for R$\gtrsim$ 100, and it is desirable to collect the light from a high redshift galaxy into as few detector pixels as possible while maintaining adequate sampling. Given the telescope diffraction limits, and the finite angular size of galaxies ($\sim$0.16 arcsec FWHM at AB=30), a spectrograph aperture should be 0.2 - 0.4 arcsec across to accept most of the light, Nyquist sampled by the detector at 0.1 - 0.2 arcsec pixels.

If only one magnification were available on both instruments, and the imager pixel size were 0.05 arcsec, and the spectrograph pixel size were 0.1 arcsec, then the set of four 4K$\times$4K mosaic detectors in the imager would subtend 800 arcsec, or 6.6 arcmin, and a single 4K$\times$4K mosaic in the spectrograph would subtend the same field. If such a large field were not available in the focal plane for each of the instruments, a suggested compromise is that the spectrograph field occupy 6.6$\times$3.2 arcmin. The spectrograph detector would use 2K$\times$4K pixels to cover the field for any one wavelength, and the dispersed spectra would spread over the whole 4K$\times$4K detector. We have assumed this arrangement in our nominal design.

1.4.2 Low Resolution–Prism Mode

To obtain spectra of the faintest objects observable by NGST, it is important to provide a low resolution spectrograph with the highest possible sensitivity per object, covering the widest possible

wavelength range, and for the largest number of objects possible per exposure, in that order of priority. The low resolution mode will determine continuum shapes and detect strong emission lines, for the determination of redshifts, star formation rates, AGN strengths etc. A prism disperser has high throughput, and can simultaneously cover a very wide wavelength range (0.6 - 5 μm).

The resolving power is adjusted to be as flat as possible over the wavelength range 0.6 - 5 μm by a selection of prism materials, and is chosen by setting the prism angles.

Low resolution dispersion is produced by a three component prism assembly, inserted into the parallel beam. In order to minimize the prism thicknesses and aberrations, all prisms were designed to have small prism angles. This required selection of materials with high dispersion. ZnSe was selected to provide low wavelength dispersion, sapphire for high wavelength dispersion and a CaF_2 final prism to flatten the resolving power in the primary 1-5μm band, produce a zero deviation condition and, help equalize the optical path over the field. The prism diameter is 70mm and the central thicknesses are 7mm (ZnSe), 7mm (Sapphire), 12mm (CaF_2) for a reflective prism assembly. Isolation of the bandpass is naturally provided by this combination; ZnSe transmission declines rapidly below 0.6 μm and sapphire above 5 μm. The sapphire prism must be cut perpendicular to the C axis to minimize bi-refringence.

Figure 1.6 shows the resulting resolving power as a function of wavelength. These values are based on resolution equal to a two-pixel (54 μm) resolution element. In the primary 1-5 μm range, the median resolving power is 47, with a low value of 23 at 2 μm, rising to 135 at 5 μm. Below 1 μm, the resolving power rises rapidly to 210 at 0.6 μm. The fraction of total energy within a resolution element in the spectral direction is very high at short wavelengths: 90% at 0.8 μm, for example. The design becomes essentially diffraction limited above 3 μm (Strehl ratio = 0.85), and the expansion of the Airy disk with wavelength reduces the enclosed energy. However, even at 5 μm, 65% of the energy is within the two-pixel resolution element. The energy contained within two pixels in the spatial direction is comparably high, providing a two-pixel resolution limit of 0.13”.

1.4.3 Low Resolution Prism Assembly

Use of very broad-band anti-reflection coatings will be important for the high index ZnSe and sapphire prisms in order to achieve high efficiency and minimize multiple reflection images. Such high transmission coatings are commercially available. Data obtained from II-VI Incorporated, for example, indicates existing coatings can produce $<$3%/surface reflection for ZnSe from 1-5 μm rising to about 10% at 0.6 μm. These coatings must also be stable at the low NGST operational temperature and must not produce any significant strain induced wavefront error.

We emphasize that this design is subject to improvement by further study. Tests should be conducted on suitably selected sample windows and prisms with appropriate coatings to assure good performance in flight. In addition, alternate materials with lower refractive indices might further increase the throughput.

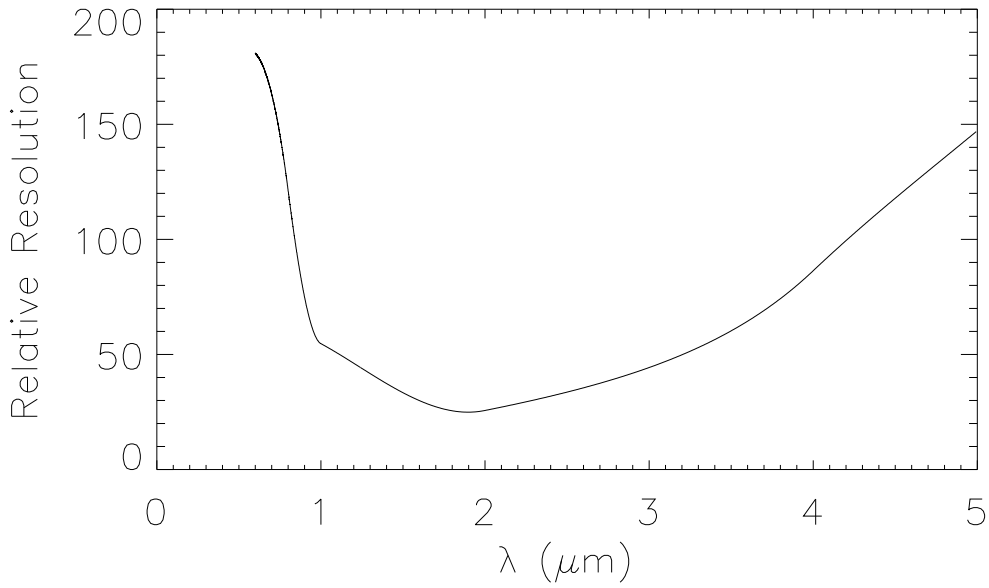

Figure 1.6: The spectral resolving power of the low resolution mode as a function of wavelength. The values are based on a two pixel (54 μm) resolution element.

1.4.4 Moderate Resolution(s) Mode

For resolving powers above $\sim$100, beyond that obtainable by a prism of reasonable thickness, we use gratings as dispersers. We compare two alternate approaches to cover the 0.6 to 5 μm range: 1) three successive first order gratings, and 2) an echelle order sorted with a Fourier Transform Spectrometer (FTS).

First Order Gratings Method

For each spectral resolving power required, the 0.6 - 5 μm range may be covered by 3 gratings, covering 2.5 - 5 μm , 1.25 - 2.5 μm , and 0.625 - 1.25 μm . Grating spacings, blaze angles and spectral lengths in mm and pixels required are shown in Table 1.2 for a reflective Littrow design with a 360 mm camera focal length, for resolving powers R=1500 and R=5000. We see that for R=1500, the spectrum can fit easily onto the 4K pixel detector length, and the full field can be observed with one object per effective dispersion row. For R=5000, the full spectrum does not fit onto the detector, and the 0.6 - 5 μm range must be divided into 12 observations for the full field.

Note that for many problems, the full spectral range may not be needed, in which case this method is more sensitive than that using the FTS order sorter below. An instrument layout for this method is shown in Figure 1.8

Mode	R	Spectrum length mm	Spectrum length pixels	Orders	Blaze angle degrees	Groove spacing lines/mm
First order	1500	54	2000	...	6.42	59.62
	5000	54×4	2000×4	...	20.56	140.45
Echelle/FTS	1500	54	2000	1-6	6.42	59.62
	5000	54	2000	4-30	20.56	39.01

Table 1.2: Characteristics of the gratings in the first order and echelle/FTS modes

Echelle With FTS Order Sorter Method.

In addition to the method of medium resolution spectroscopy using several first order gratings, we have investigated covering the 0.6 - 5 μm wavelength range in a single observation using a low order echelle grating, which can cover this range in 6 orders. To enable a large number of objects to be observed simultaneously, the order sorter should be non-dispersive. We have thus chosen an IFTS as an order sorter. We use the minimum possible number of steps to avoid additional read noise from the required multiple measurements. Two detectors are required to use all the light and maintain efficiency. This provides redundancy and excellent immunity from cosmic rays. The echelle/FTS combination would be used in series with the microshutter field selector, as would all the spectroscopic modes described.

As discussed below, this more complex method is not justified in order to obtain improved sensitivity for the primary spectroscopic modes at R$\sim$40 and R$\sim$1500. The advantages of this method are that it enables a higher spectral resolution (R$\sim$5000) mode, and a full-field low spectral resolution imaging mode. This imaging mode provides a sensitive backup to the NIR imaging camera, thus greatly reducing risk in the overall NGST mission.

The sensitivity advantage of this method compared to successive observations with first order gratings depends on the number (N) of successive observations needed. For very long observations where the sensitivity is not limited by any additional read noise from the multiple FTS scan positions, the sensitivity advantage is $F = \sqrt{N/2}$, for equal throughput. For R$\lesssim$2000, where the first order spectra can fit on the detector, N=3, and F=1.22. This small advantage of 20% improvement in sensitivity would be lost in the FTS at the beamsplitters and mirrors. In addition, for shorter total exposures than $\sim$40,000 sec, individual readouts of the FTS step scans would have to be more frequent than that necessary for cosmic ray removal. This additional read noise would dominate the overall background for R$>$50, so that the sensitivity would be lower than for the successive first order grating observations.

At higher resolutions, for example for R=5000, where the number of successive first order grating exposures (N) for full spectral and field coverage would be 12, F=2.3, so a factor 2.4 fainter object or higher S/N could be reached in the same time, or the same S/N could be reached on a given object in a factor 6 less exposure time, using the echelle/FTS. In order to fit these higher

resolution spectra on the detector, orders 4 to 30 would be used, requiring 60 to 90 scan steps with the FTS.

As a backup imaging mode, a mirror may be moved into the beam in place of the echelle. Then the FTS can be used as a multiband imager with all the microshutter pixels open, with a flexible number of bands and within band sampling controlled by the scan range and number of scan steps. It would be more sensitive than successive multi-filter imaging by observing the total wavelength band all the time. Sensitivity would not be lost by the addition of read noise from the scan positions, since at very low spectral resolution the background would be dominated by zodiacal light. However, it would have a pixel scale on the sky a factor 2 - 4 coarser than the prime imager.

An optical layout including the echelle/FTS is shown in Figure 1.9, and its integration with NGST is shown in Figure 1.10. The echelle characteristics and field coverage for full spectra are shown in Table 1.2.

1.4.5 Sensitivity Estimates For Different Modes.

A crucial advantage of the proposed spectrograph design is efficiency. In addition to providing the multiplexing benefit of wide simultaneous wavelength coverage, the prism-based design offers very high throughput. In the low resolution mode, optical losses come from reflection losses at the prism surfaces (6) and reflections at the mirrors. The low index prisms have $<$3% loss per surface even without anti-reflective (AR) coating, while the high index ZnSe prism can be AR coated to $<$3% loss per surface over at least the 1-5 μm range (measured data from II-VI Corporation). Mirror reflectivities are $>$99% in this band. Hence, the throughput of the optical components in the low resolution mode is thus expected to be $>$80%. No combination of grating plus order sorting filter can match this performance over even one octave of wavelength coverage.

The medium resolution mode substitutes one first order grating for the prism, with an estimated peak efficiency of 65% (Hyperfine Inc., private communication). To cover the full spectral range of 0.6 - 5 μm we divide the total exposure time by 3. (For the alternate case of the echelle with FTS order sorter, full wavelength coverage is achieved with only the one grating, but for long exposure times, the sensitivity is the same to within $\sim$20%.)

Raytraces indicate that $>$70-80% of the energy incident at the entrance mask plane from a point source can be captured within a nominal 2×2 pixel resolution element out to wavelengths of 2.5-3.0 μm. However, to include most of the flux from typical faint galaxies, to account for centering, and to reduce diffraction losses at longer wavelengths, we would expect that a typical entrance aperture might be chosen to be $\sim2\times3$ pixels. We anticipate end-to-end efficiencies (within 2×3 pixels, including detector quantum efficiency) up to 50-55% in the low resolution mode near 1 μm and up to $>$40% in the medium resolution mode.

Based on these estimates, we have calculated the minimum detectable flux at a signal to noise of 10 per spectral resolution element, assuming total exposure times of 10^4 seconds and 10^5 seconds. The results are critically dependent on the assumed detector dark current and readout parameters

and (for the low res mode) zodiacal light intensity, due to the extremely background-limited nature of the calculations. The resulting 10 σ source detection limits in 10^5 seconds are in the range of 4 to 10 nJy and 300 nJy, respectively, for the two modes (assuming dark current of 0.02 e/pix/sec and 4 e rms read noise per readout). The results are shown in Figure 1.7.

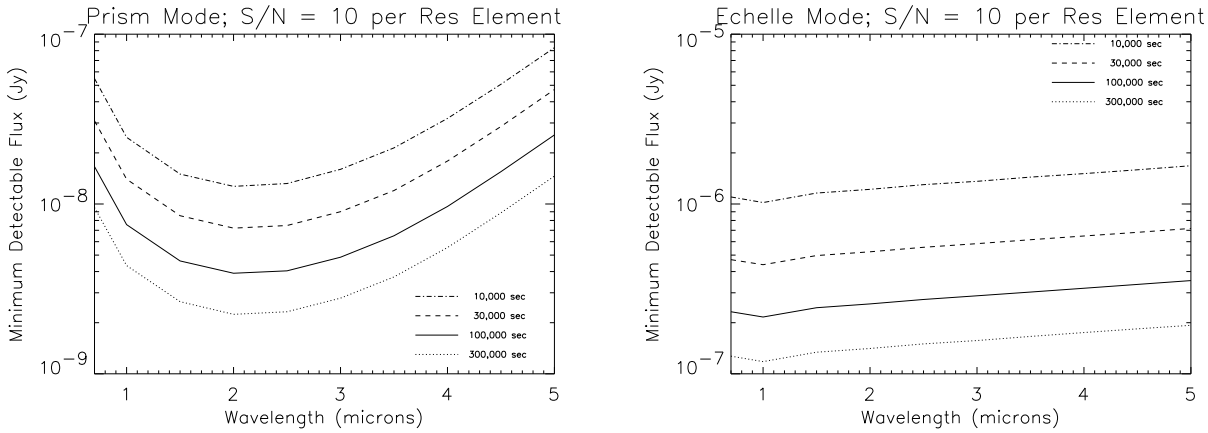

Figure 1.7: Minimum detectable flux in the spectrograph per spectral resolution element, for S/N = 10, for exposure times between 10^4 and 3×10^5 sec. (a) Low resolution prism mode. (b) Medium resolution gratings or echelle mode.

We emphasize the sensitive dependence of the results on detector assumptions. The critical point to make is that, whatever detector performance and aperture size NGST achieves, the sensitivity of a high throughput spectrograph design that puts the bulk of the energy into a few pixel resolution elements can not be surpassed.

1.4.6 Dithering And Readout Noise.

Another distinguishing feature between the first order gratings and the echelle/FTS methods is their ability to utilize dithering to flat field, (as described in the calibration section,) to subsample the spectral and spatial pixellation, and to remove saturated cosmic rays. For the first order gratings, individual exposures with the total exposure time are essentially independent, and so dithering can be used between them. For the echelle/FTS, the entire set of FTS scan positions must be made and read out before any dithering motion can be allowed.

By multiple non-destructive readouts during an exposure, the slope of the counts vs time plot can be measured and the effective read noise reduced compared to reading out only at the end of the integration[14],[15]. This method was used by NICMOS. Cosmic ray events during an exposure can be removed by measuring the slope on either side of the cosmic ray jump. This allows very long exposures provided saturation does not occur, which will be easier for spectroscopy than imaging. In a single exposure of 1000 sec, 10% of the pixels would suffer a cosmic ray hit, and 1%

would suffer multiple hits. The reduction in read noise for N non-destructive reads compared to a single read is $\sqrt{N/6}$. The factor 6 is comprised of a factor 2 due to differencing the samples, and a factor 3 due to sampling all along the slope rather than only at the ends [16]. In the [14] example, their assumed 15 electrons (hereafter: els) rms read noise per read is reduced to 6 els rms by taking 64 samples. Similarly, currently measured read noise values of 4 els rms should be reduced to 1.6 els rms by taking 64 reads per slope. Also, with this method the data from each set of reads up the ramp would be processed on board, dramatically reducing the telemetry requirements.

Compare for example an observation with total exposure time of 10000 sec taken by the two methods at R=1500. The three first order gratings each get 3300 sec to cover the wavelength range. For 5 dither positions each, the individual exposures are 660 sec. The 1.6 els rms effective read noise is small compared with the $\sqrt{660 \times 0.02} = 3.6$ els rms noise from the dark current. In comparison, the echelle/FTS would get 2000 sec per dither position. To cleanly sort the 6 orders of the echelle, assume we need 18 FTS steps, giving 110 sec per step and therefore readout. We have 1.6 els rms effective read noise per scan position, or $1.6 \times \sqrt{18} = 6.8$ els effective read noise over the scan range, compared to the $\sqrt{2000 \times 0.02} = 6.3$ els rms noise from the dark current, so that the added read noise from reading out the multiple scan positions has reduced the sensitivity of the echelle/FTS method by a factor $\sim$1.4. We note however, that at this readout frequency, a significant burden would be placed on the telemetry, and that accomplishing the multiple non-destructive reads in 110 sec may be difficult. We see that for total exposures significantly longer than 10000 sec with 5 dither positions, the echelle/FTS remains dark noise limited, and does not suffer from sensitivity reduction due to multiple scan position readouts.

1.4.7 Optical Requirements For A Field Selector

In order to cover the required broad spectral band of NGST, we need an input selector which can operate over the broad spectral range, can select objects at random positions in the field. In this section, we describe the requirements for the field selector for a MOS on NGST.

The selection of a set of objects for spectroscopic observation requires a prior image of the area of the sky to be studied. This image could either be obtained with the NGST camera, or with the spectrometer in camera mode with all shutters open. In general, the objects for study will selected on the basis of their colors in multiband imaging studies. This approach allows the high redshift candidates to be separated from the far more numerous foreground objects. Therefore, the microshutter array must be able to select objects based on other NGST images, and in some cases, based on images with other facilities.

The pixels in the microshutter array are in a regular grid, and objects on the sky are randomly positioned with respect to this pattern. If the object is centered in the pixel we will open an odd number of pixels, and if the object in on the border between two pixels we will open an even number.

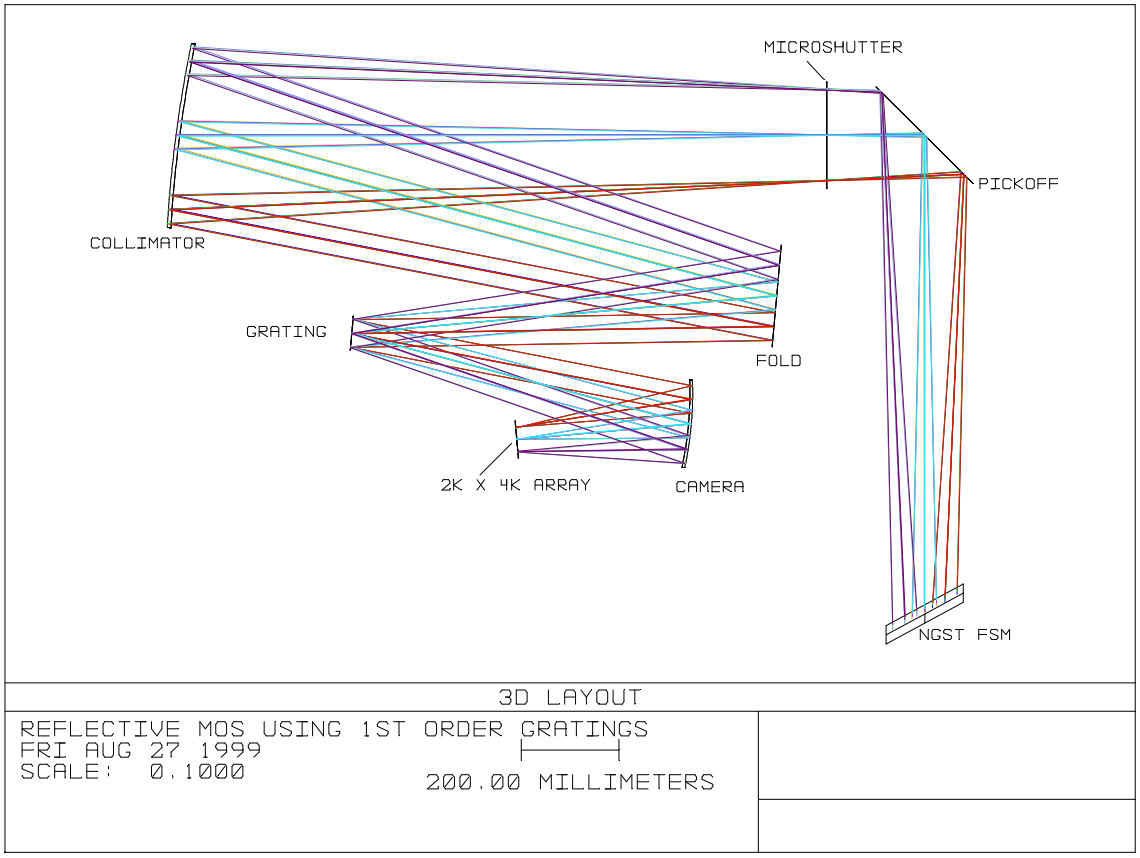

Figure 1.8: Instrument optical layout for the first order grating/prism method, showing half the 2K×4K field. The full field would be provided either by widening the field or by splitting it into two sections, depending on subsequent aberration analyses and redundency issues. A reflective prism mode is incorporated as a position on a grating wheel.

Pixel Size

The design of a field selection device for NGST is complicated by the wide wavelength range over which it must operate, 0.6 to 5.0 μm . Over this range, the size of a diffraction limited image changes by a factor of 8. Moreover, the natural backgrounds vary by over an order of magnitude over this range, and the effects of this background on speed of acquiring a spectrum varies with spectral resolution; at sufficiently high resolution, the system will no longer be background limited. From our discussions of galaxy size earlier, with galaxies at AB=30 having half light diameters around 0.16 arcsec, and considering the point source diffraction size, pixels of 100 μm will subtend 0.093 arcsec, and so will provide good sampling of the images while covering a large field of view. To cover the large NGST field of view that we have assumed to be available, a 2000×4000 array of 100 μm pixels (matched to the diffraction disk at 4 μm) is required, a number which is feasible

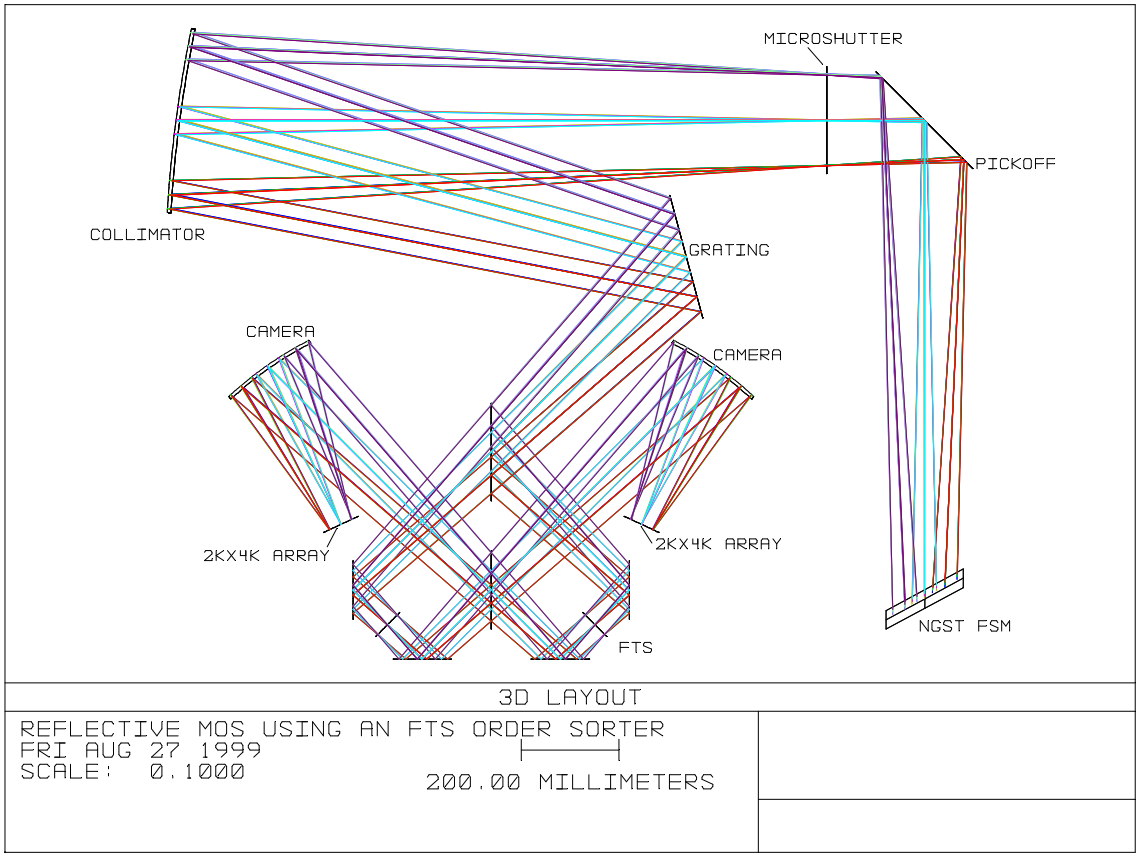

Figure 1.9: Instrument layout for the echelle/FTS/prism method, showing half the field as in 1.8.

to construct. If the pixels are matched to the 1 μm disk, the required 10000×20000 array of 20 μm pixels is not within technical reach in the NGST timescale. Thus, practical considerations drive us to the 100 μm pixels.

Cryogenic Operation

In order to maintain low background in the spectrometer, the field selector must operate at sufficiently low temperature that its thermal emission is negligible compared to sky background. An operating temperature of 40 K will meet these requirements for a long wavelength cutoff of 5 μm . However, for simplicity and in case longer wavelength operation is required, we have adopted a requirement of 30 K for microshutter operation.

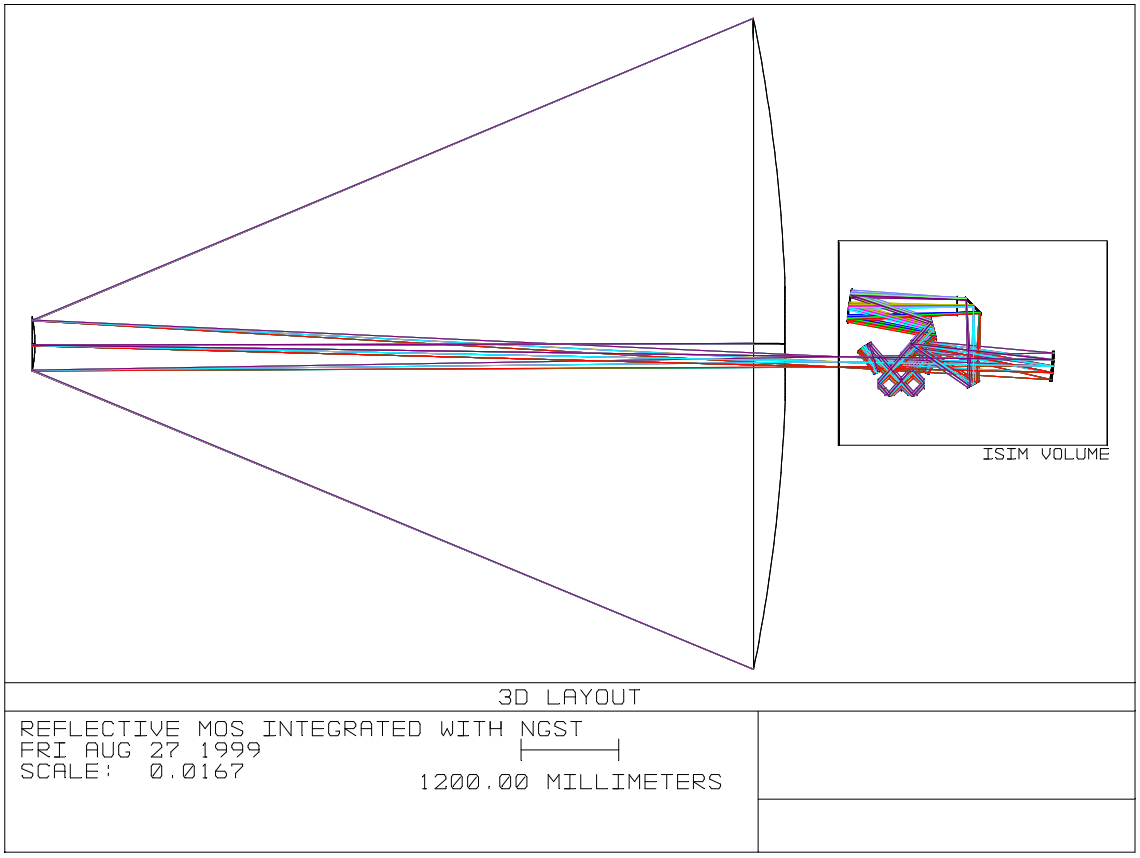

Figure 1.10: Optical ray trace of a possible MOS Design integrated with the NGST.

Fill Factor

The goal for our microshutter array is to have the largest possible filling factor. Given the necessity for structural support for the individual shutters and for electronics to actuate each one, we have adopted a requirement of 80% for filling factor. This is soft requirement; if we can achieve better filling, we will strive to achieve it. Also, if the best filling factor possible is somewhat smaller than 80%, the device is still useful. It may also be possible to increase the filling factor by use of an array of micro lenses or Winston cones.

Other Requirements

In addition to the basic optical requirements cited above, there are practical requirements which further limit shutter designs. First, the mechanism and suspension required to define the motion of the shutter during actuation must be small. Second, the actuator itself must be compact and have low power dissipation.

Field of view	$3.2' \times 6.3'$
Number of Pixels	2000 x 4000
Pixel size	100 x 100 μm
Addressing	Any pixel on any row
Actuation time	less than 30 s (TBD)
Operating temperature	30 K
Operating Power	less than 1 mW average (TBD)
Fill Factor	more than 80%

Table 1.3: A practical input selector for a MOS for NGST must meet a number of requirements, shown in Table 1.4.7.

Chapter 2

Engineering: Development Of Microshutters

2.1 Overview

In this study, we have developed a concept for a new optical component, a densely packed microshutter array, to be used as a programmable field selector for a Multi-Object Spectrometer on NGST. This transmissive field selection device has fundamental advantages over reflective versions. The transmissive version has excellent immunity to scattered light from bright objects in the field; only light incident on the open apertures can reach the focal plane. In the case of a reflective selector, the diffracted light from the edges of illuminated but unselected mirrors in the field can enter the instrument. The transmissive selector has a great advantage in optical design. For a reflective selector to work, it must be placed in an image plane. In order to have access to the reflected beam, it must be tilted with respect to the input axis, requiring a tilted image plane. This in turn requires that the detector image plane be tilted with respect to the principal ray of the system. This complicates the already difficult problem of designing a large field spectrometer for NGST. Finally, the performance of a transmissive selector is insensitive to the figure or surface finish of the shutters, where the reflective version requires a good surface figure.

This report describes the first design for a programmable transmission mask for a MOS. In our study, we have:

- developed the concept for the microshutter array, including individual shutter operation and the selection and actuation mechanism for essentially random access addressing.
- measured strength and stiffness of candidate materials for shutters, selected materials for fabrication, and optimized their mechanical design.
- tested the mechanical properties of individual shutters, and built and actuated small microshutter arrays

- developed plans for the production of larger. arrays to be fabricated with integrated shutter selection electronics using photolithographic processes.

Pursuing this development program aggressively, we can demonstrate technical readiness with a full scale microshutter array by the Apr. 2001 NGST instrument selection.

2.2 Background

The development of techniques for production of micro electro mechanical systems (MEMS) has provided us with tools for the production of randomly addressable field selectors for multi object spectrometer (MOS) applications.

Initial instrument definition work for Next Generation Space Telescope (NGST) gave a strong boost to efforts to produce programmable field selectors for MOS applications, specifically for the NGST near infrared spectrometer[17]. These near-infrared field selection devices must be cooled to cryogenic temperatures to provide the required low background. Inspired by the development of the DMD (Digital Micromirror Devices) by Texas Instruments, two teams are currently developing micromirror arrays for the NGST[18, 19]. The task is extremely challenging and devices developed so far remain complex and expensive to manufacture, and have the problems of implementation described above.

An alternative approach to field selection is the use of microshutter arrays [20]. The shutters should offer significant performance benefits for applications requiring high-contrast imaging, and, as transmission devices, offer important advantages in optical design and layout over their reflective counterparts. However, no large arrays of microshutters have been developed. Arrays have been built by CSEM of Neuchatel, Switzerland, but they have low area filling factor and small number of shutters (`http://www.csem.ch/microsystems/`). These devices employ a resonant excitation technique to open the shutters and are designed for operation at room temperature.

We have developed a concept for a transmissive field selector, and have fabricated and tested demonstration arrays. This concept can be developed into a large fully addressable microshutter array of elements well-matched to the NGST point spread function (100 μm typical dimension) with high area filling factor (80% or better for the ratio of shutter area to the total area).

This microshutter concept grew out of designs for arrays of thermal detectors developed at GSFC. The GSFC Detector System Branch has experience manufacturing pop-up bolometers that require profiling thin Si wafers with flexures that allow bending of the devices out of plane. These thin suspension structures are flexible enough on one hand to be bent at 90° angle, on the other they are stiff enough to support a relatively large area membrane. This geometry lends itself to the production of microshutter arrays. Our microshutters are an extension of this basic concept, with significant new ideas which were required for addressing and actuation.

The production of these devices offered several technical challenges. First, our microshutters require large angles of rotation of the individual microelements (90°) as compared to micromirrors ($\sim$15°). Also, in micromirror arrays, the space behind the mirrors is available for the actuation

structures and addressing electronics, where in microshutter design, all these must be fabricated in the tiny support structures between the blades and/or on the shutter blades themselves.

Our design successfully addresses these challenges. The shutters can reliably rotate through the required 90°, and our novel selection and actuation mechanism, the doubleshutter, provides a practical solution to random access addressing of the high efficiency shutter.

Although these microshutters are being developed as cryogenic field selectors for NGST, they can also be used at optical wavelengths on the ground-based telescopes and in other applications where field selection devices are required, such as projection television. Other possible applications are mass–spectroscopy and laser ranging. In mass- spectroscopy, microshutters can be efficiently used for modulation of the ion source and spatial modulation of the detector. In laser ranging applications, they can provide fast-changing attenuation of the optical signal that would help to expand the dynamic range of operation.

2.3 Microshutter Concept

The requirements of large deflection angles and high efficiency close packing of shutters are solved in a unique asymmetric suspension of the microshutter blades. The solution for the actuation mechanism to satisfy the requirements of high density packing and low power dissipation is what we call double shutter scheme with a DRAM (dynamic random access memory) type addressing circuit. In the this section we will discribe details of the suspension design and actuation mechanism.

2.3.1 Torsion Beam Suspension

Key requirements of the shutter design are that it accomplish the required 90° rotation, has a long operational life, and a large area filling factor, consistent with random access addressing. The design must provide space for the selection electronics and actuation mechanism.

Our shutters are designed with asymmetric suspension on a torsion bar attached to the middle of the edge of the shutter (Fig. 2.1). This design allows us to use the entire width of the shutter for the torsion bar, reducing stresses in the bar. Mechanical analysis and tests proved that this design allows full deflection of the microblade out of the light path[21]. Although such suspensions have been used in MEMS technology before [22, 23, 24], previously developed devices did not simultaneously require tight packing and large deflection angles.

An important advantage of our design is that it is simple to manufacture. It doesn't require complex multicomponent cells; the whole shutter array can be manufactured by photolithography from one single membrane, and is easily scalable to larger sizes.

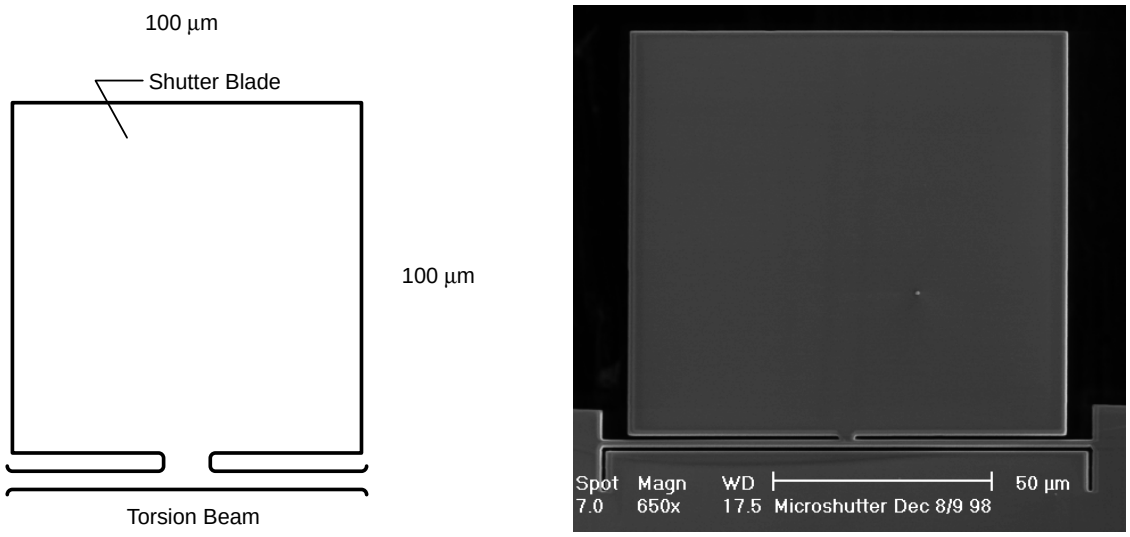

Figure 2.1: a) Schematic of the basic shutter design. b) Scanning electron micrograph of a micromachined shutter.

2.3.2 Actuation

The actuation schemeis a novel aspect of our microshutter design. After examining several candidate solutions, we selected the scheme which we call the "doubleshutter". Doubleshutter actuation allows us to transform the motion of a large structure, the membrane itself, into micromotion of the selected shutters (Fig. 2.2). To implement this, two identical microshutter arrays are rotated 180°with respect to each other and brought into close physical contact. Addressing and selecting is performed electronically by applying a voltage between a shutter blade and its counterpart on the actuation membrane. This force is attractive independent of the polarity of the applied field. Once a blade is selected and engaged, the entire actuation shutter array is moved by the actuators located outside of the active area, opening all engaged shutters. De-selection will cause an open shutter to elastically return to its closed position (Fig. 2.2).

In this design, the required mechanical components are relatively simple in design and easy to fabricate. Both shutter arrays are made from a thin single membrane with embedded microcircuits for shutter engagement and appropriate optical coatings as required. The low stress of the torsion bars even at large deflection angles allows the use of relatively low voltages for shutter engagement, at the level of $\sim$20 V. We have tested this actuation scheme on a single element shutter (Fig. 2.2) and a 3 x 3 array(Fig. 2.3). The next step will be to design and manufacture larger size arrays using photolithographic processes, initially with 128×128 elements.

2.3.3 Selection Electronics

There are two approaches to shutter actuation selection:

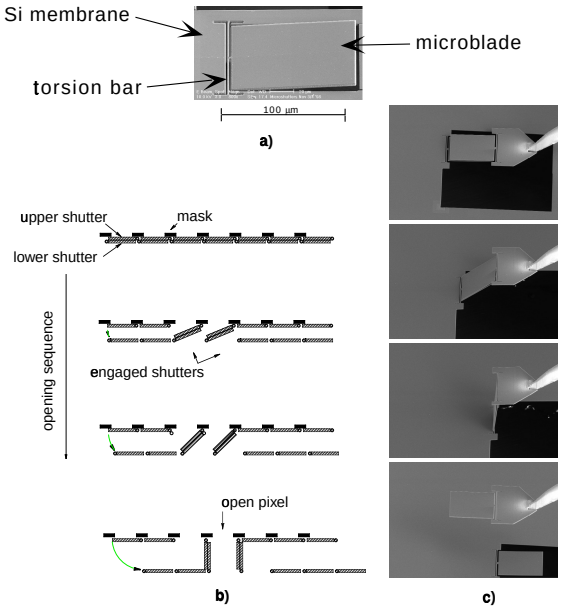

Figure 2.2: a) SEM image of a single shutter blade, b)Sequence of the microshutter opening (side view). Microshutter blades are represented by the shaded rectangles. Shaded circles are torsion bars. Two blades are engaged to have one pixel open, c) Opening sequence of the single shutter model. Shutters first are brought to close contact, and a voltage is applied to engage the shutters. The lower shutter is attached to the bulk of a membrane, the upper shutter is welded to a needle-manipulator. The upper shutter is moved along the arc formed by the radius-vector connecting their torsion bars. Frame three shows the shutter blades at 90° to the membrane (full open position). After the voltage is reset, shutters return to initial position (frame four).

- SRAM (Static); A voltage is latched on each selected shutter, using a flip-flop per cell. So far, we have no viable design, because the large number of transistors necessary cannot be fitted on frame using available technology. It would be an electronically straightforward technique given adequate chip area.

- DRAM (Dynamic); A voltage is appied to the selected shutter. The voltage is refreshed after a short time. This requires shutters to hold charge for a time determined by the refresh cycle, requiring their leakage resistance to be $\sim 10^9\Omega$ for practical operation.

Our preferred solution is to use dynamic addressing, refreshing the voltage on each selected microshutter sequentially. Each engaged shutter can be considered as a tiny capacitor. Once it is charged by the addressing circuit , the deposited charge will attract the blades to each other. We expect the leakage currents from the shutters to be small, so the hold time of the shutters will be long enough to have acceptably low required refresh rate. This multiplexing and dynamic addressing can be accomplished with a single FET per unit cell, resulting in simple on-chip circuitry which

can be fit on the interstitial structures. Address selectors must lie on two perpendicular sides of the array.

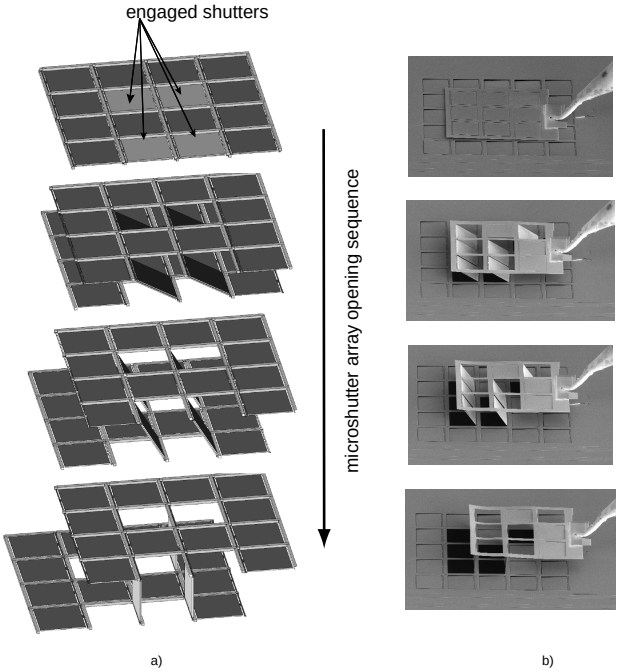

Figure 2.3: a) 3D sequence of the double-shutter actuation mechanism, b) SEM images of five by five microshutter array.

2.4 Development Process With Rapid Prototyping

Following the development of the shutter concept, our development program moved on to the production of a detailed mechanical design of the shutter element, actuation mechanism design, measurement of the mechanical performance of the device, and iteration on the design. This design and optimization was the primary objective of this study. Designs were developed and studied using both analytic and finite element modeling techniques. Our approach to production and test, the use of the programmable Focused Ion Beam(FEI) facility, allowed rapid prototyping and test. Below, we describe this process, and the results achieved during the study. The final section describes our plans for the next phase, the transfer of the design to a photolithographic process.

2.4.1 Manufacturing And Test Facilities

All microshutter manufacturing and experiments were carried out in a FEI 620 focused ion beam milling machine at the Lab for Ion Beam Research and Application (LIBRA) of the University of Maryland. This machine has proven to be a very useful tool both for device production and *in situ* testing of the manufactured devices [21]. The FEI 620 is a dual beam machine, with an ion and electron column, permitting ion milling and *in situ* scanning electron microscopy. Ion milling can be performed with ion beam spot sizes in the range from 20nm to 1 μm . Machining rates in Silicon from $10^{-3}\,\mu m^3 s^{-1}$ to $10\,\mu m^3 s^{-1}$. The machine is also equipped with a micro-manipulator needle and has the capability of depositing Platinum(Pt) by ion-induced MOCVD. This combination turned out to be a perfect tool for production and testing of the microshutters, offering the following capabilities:

- Structures can be machined and measured virtually in real time.
- Tests involving bending and moving can be done *in situ* using the manipulator needle.
- The shutter response time to a mechanical impulse can be measured by focusing an electron beam on the shutter edge and observing secondary electron current as a function of time.
- One can machine electrodes, weld them to a needle by depositing Pt and use it to apply electrical forces to a machined microstructure.
- One can machine MEMS structures, weld them to the needle, and use them for tests.

An important issue in the design of the shutters is to understand the mechanical reliability of the manufactured structures and determine their failure mechanisms. We did analytical and finite element analyses of the stress distribution and maximal stresses in the shutters to aid in the design of the shutter and selection of materials (see section 2.4.2), and carried out tests of the shutters to determine their mechanical characteristics and failure modes. This production and test capability truly enabled the rapid development we have made in the development of these devices. It will remain an important tool for mechanical characterization of the photolithographically produced devices in our next phase of development.

2.4.2 Mechanical Analysis And Material Properties

Accurate mechanical analysis of a component relies on accurate descriptions of its material properties, geometry, and boundary conditions. The key material properties for such analyses are the stiffness of the material, which relates the stress in the material to any applied strain, and the strength of the material, which establishes the stress level at which failure becomes probable. Research has shown that the elastic properties of materials used in micromechanical components are usually well described by their bulk properties, but estimates of strength require test of a large

number of samples of similar geometry to the object of interest [25] [26]. The strength of the small samples are typically much higher than in macroscopic samples and show a much larger range of failure stresses, set by the presence or absence of defects in a sample, consistent with brittle fracture theory. Any successful design must allow for the full distrbution of failure stresses.

In the following subsection, we describe simplified models and tests of a cantilever beam which we used to determine the Young's Modulus for our samples. This step was useful for validating our experimental techniques, and finding discrepancies between the properties of bulk and microscopic samples. Next we present a technique to determine the fracture strength of both single crystal silicon and silicon nitride. The results from these two subsections were used as inputs to our microshutter design efforts.

Material Stiffness Some researchers [27, 28, 29] have used bending tests to determine the stiffness and fracture strength of silicon membranes. In these testss, the membranes were more than 10 μm thick. Forces greater than .01 Newtons induced reasonable bending and failure. The membranes used in this study are .5μm and 2 μm thick. The corresponding forces are significantly smaller than 0.01 Newtons. Commercially available force transducers can not resolve forces at such a low magnitude. Thus we have chosen a vibration test method to determine the Young's modulus.

In the vibration test, the ion beam is used to fabricate long cantilever beams of total length L_t in a "T" shape as shown in Fig. 2.4. At the fixed end, the beam has a narrow width w_a, which extends to a length L_a. The remaining portion of the beam of length L_b is wider with width w_b. The total length is denoted as $L_t = L_a + L_b$, and is aligned, in the case of the Si, with the <110> crystalline direction. The purpose of this configuration is to yield a cantilever mass/spring system, whose first natural frequency can be measured and computed analytically. The mass at the end can be increased to reduce the frequency to a range that can be easily measured.

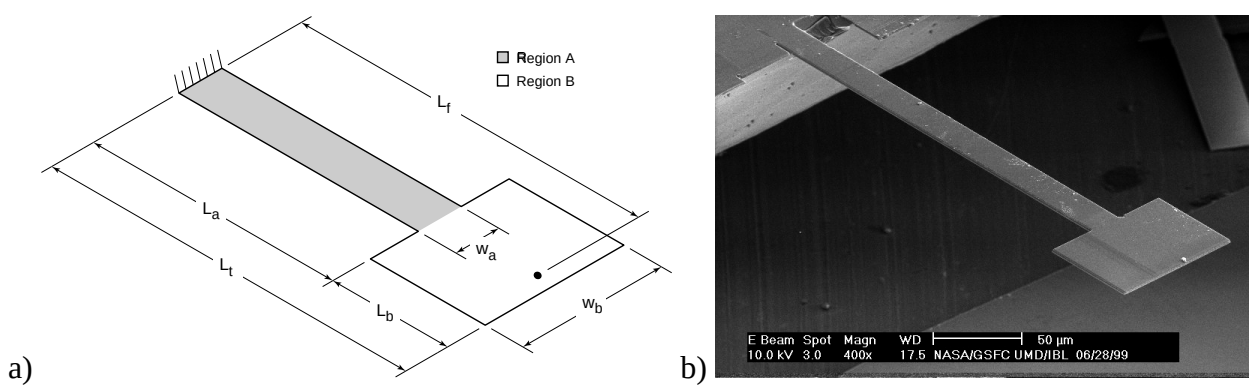

Figure 2.4: a) Schematic drawing of the cantilever beam vibration test specimen. b) Scanning electron micro-graph of machined cantilever beam.

In the experimental setup, the beam is pushed vertically with a needle and released. The ap-

proximate natural frequency is measured as described above. Subsequently, an electrode is placed in close proximity to the end of the beam and a periodic voltage is applied. The frequency of the voltage is varied over a small range around the approximate value previously determined. The response is monitored, and the frequency of peak displacement is recorded.

The natural frequency of a cantilever spring mass system can be expressed as [30, 31]

$$f = \frac{1}{2\pi}\sqrt{\frac{3EI}{L^3(m_b + C_1 m_a)}} \tag{2.1}$$

where the constant C_1 equals 0.2357, f is the cyclic natural frequency in Hz, $L = L_a + L_b/2$ is the cantilever length to the center of the end mass, E is the Young's modulus, $m_a = \rho w_a t L_a$ is the mass of region A, and $m_b = \rho w_b t L_b$ is the mass of region B, where ρ is the mass density. The area moment of inertia I equals $(w_a t^3)/12$, where w_a is the region A width, and t is the membrane thickness.

Hence, the Young's modulus can be solved for

$$E = \frac{4\pi^2 f^2 L^3 (m_b + C_1 m_a)}{3I}. \tag{2.2}$$

A silicon cantilever beam with dimensions of $L_a = 250\ \mu m$, $w_a = 20\ \mu m$, $L_b = 80\ \mu m$, $w_b = 70\ \mu m$, and thickness $t = 1.9\ \mu m$ aligned with the <110> crystalline direction was fabricated and tested. The natural frequency was measured as described above and determined to be $f =$ 12600 Hz. Computed effective Young's modulus $E = 155$ GPa. This value is about 12% lower than the value of $E = 176$ GPa reported in [32].

Here we note that the Young's modulus is highly sensitive to the thickness and cross sectional shape used in the calculation. The thickness of $t = 1.9\ \mu m$ was measured from scanning electron microscope images. Because $E \sim t^2$ any error in t is magnified in E. We also assumed a rectangular cross sectional shape in these calculations, and in fact the shape is rounded at the corners, which will compound the error. While the chromium coating only occupies about 1% of the total volume, the modulus is significantly lower than that of silicon, and will result in a lower effective modulus. The above two sources of error combined with the potential for error introduced by using simplified equations are likely to account for the observed discrepancy with bulk properties for Si.

In a second experiment, a silicon nitride simple cantilever beam consisting of a single width w_a was fabricated and tested. The dimensions of the beam were $L_a = 205\ \mu m$, $w_a = 9\ \mu m$, and thickness $t = 0.55\ \mu m$. The natural frequency was observed to be $f = 17800$ Hz, and the Young's modulus was calculated as $E = 220$ GPa. This value is about 43% lower than the value of $E =$ 385 GPa reported in [33].

The difference in this case is much more significant than for silicon. Again the largest source of error is likely due to the thickness and cross sectional shape. The silicon nitride thickness of 0.55 μm is almost 3.5 times less than that of the silicon, but the resolution of the measurement technique is the same. Hence, the relative error introduced by the resolution limit is greater for

the thinner membrane. Given all the geometric uncertainties, the measure modulus of the silicon nitride film was lower than bulk values. This silicon nitride was fabricated using a chemical vapor deposition process which is known to result in lower density and stiffness than the bulk properties. As a result the bulk value of $E = 385$ GPa is likely to be too high in this case, so we adopted our experimentally determined value of modulus for the nitride films.

Material Strength Both silicon and silicon nitride considered for the shutter design are brittle. That is, the material strengths strongly depend on defect distribution. The number of defects decreases with the material volume. The average strength of a sample and its variance increases with decreasing sample size; the strength will vary from sample to sample, depending on the defect distribution. Consequently, the material strength is a function of both design and processing.

Wilson et. al. [28] presented strengths in the range of $1-2$ GPa for micro-cantilever silicon beams with thickness of 30 μm. In our work, the membrane thicknesses are 2.0μm and 0.5 μm, and the membranes are coated with metallic substances. This will lead to strengths for the shutter design that are different than values presented elsewhere. The membranes are also so thin that simple cantilever beam tests tend to bend beyond 90° before failure, making it difficult to ascertain strength.

In order to determine the material strength, we again use the "T" shaped beam shown in Fig. 2.4. Only in this case we select $w_b >> w_a$ such that region B is rigid relative to region A.

In the experiment, we push the large blade through a rotation θ. The peak stress occurs at the fixed end and is $\sigma = Mc/I$, where c is the half thickness of the membrane. We find

$$\sigma = \frac{\theta E c}{L_a\left(1-\frac{1}{2n}\right)}. \tag{2.3}$$

The above equations become less sensitive to the force position for large n. Even for smaller $n > 2$, a small change in n has little effect on the results. Consequently, we do not need the precise location of the force L_f to get reasonably accurate measures of stress.

Based on the above estimates, silicon cantilever "T" beams with dimensions of $L_a = 6.55$ μm, $w_a = 6.25$ μm, $L_b = 60$ μm, $w_b = 30$ μm, and thickness $t = 1.9$ μm were fabricated and tested according to the above procedure. A deformed cantilever specimen is shown in Fig. 2.5a. The maximum rotation θ of region B was measured just prior to failure. Preliminary results indicate that the angle of rotation at failure is slightly greater than 20°. A fracture surface is shown in Fig. 2.5b. The corresponding failure stress computed using equation (2.3) is $\sigma_f = 9.4$ GPa.

The same experiment was completed for silicon nitride with $L_a = 2.3$ μm, $w_a = 2.1$ μm, $L_b = 20$ μm, $w_b = 10$ μm, and thickness $t = 0.55$ μm. All of the tests failed at angles much greater than 20°. Consequently, for the current set of results, the angle may be too large for the equations presented above. However, we know that the specimens fail at angles greater than 20°. As a result we may choose 20°as a lower limit to yield a conservative estimate of the strength. The corresponding failure stress for silicon nitride computed using equation (2.3) is $\sigma_f = 16.9$ GPa.

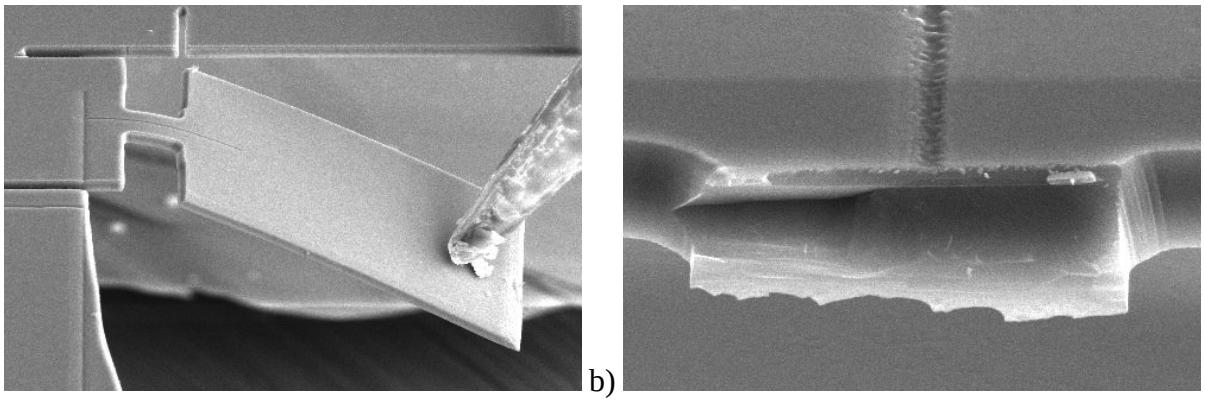

Figure 2.5: Scanning Electron Migrographs of a silicon "T" beam with dimensions of $L_a = 6.55\ \mu m$, $w_a = 6.25\ \mu m$, $L_b = 60\ \mu m$, $w_b = 30\ \mu m$, and thickness $t = 1.9\ \mu m$. a) SEM of "T" beam bending prior to failure. b) Fracture surface after failure.

The larger than expected angles of rotation may be due to the shape of the membrane at the fixed end of region A. As shown in Fig. 2.5a, the base of region A is attached to the surrounding membrane, which was cut to the same width as region B. If the base membrane was left uncut, the stiffness would increase, and the specimen would fail at lower angles. In either case the important value of rotation is the relative difference between the base and end rotations of region A.

The above failure stress values are on the same order as those reported by Johansson et. al.[34], but much greater than the values presented by Wilson et. al.[28]. Consistent with fracture theory, smaller volume results in fewer defects and higher strengths. Here we have thicknesses less than one tenth of the thicknesses used by Wilson et. al.[28]. The coating material may also provide a small increase of the strength [34].

For our study, we took the minimum observed failure stress as the input to our design. As we move to the larger scale arrays, we must measure the full failure distribution to allow accurate estimates of failure probability.

Single Shutter Tests The FEI 620 machine setup allowed very quick turnaround in tests which, in turn, resulted in a fast development from the idea inception to the implementation, test, and refinement of the design. Within a few months we were able to progress from scratch to a fully operational single element microshutter.

In our initial tests, microshutters with a variety of torsion beam geometries and mounting configurations were evaluated. These tests showed that careful mechanical design was necessary to avoid stress concentrations, especially in the areas where the torsion beam is attached to the support structure. Having selected a low stress geometry, the single shutters survived the maximum possible rotation of 180°without mechanical failure, consistent with predictions of finite element analysis based on measured material properties [21].

An important aspect of the tests was to study different materials. In initial tests, shutters were

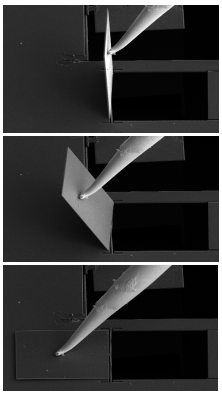

Figure 2.6: 180°rotation of the shutter blade.

made from a 2μm thick single crystal Silicon membrane. We later acquired thinner SiN membrane (about 0.5 μm thickness) and manufactured and tested shutters mode from this material. Both materials demonstarated adequate strength to withstand stresses while rotating the microshutter out of the plane (Fig. 2.6). The selection of the material for shutters for the NGST applications will be made basis of ease of fabrication, performance and reliability. This final selection will be made in the next phase of the development program.

Microshutters with torsion beams of different widths were studied to determine the ultimate mechanical stress limits. These tests showed that there is significant strength margin in our chosen mechanical design, consistent with the results of our analytical studies and FEA modeling.

Resonant oscillation tests on a small sample of devices also demonstrated that the microshutters are robust and can withstand up to 10^6 large amplitude deflections without failure. More extensive tests of the mechanical reliability will be carried out on the arrays.

Mechanical Summary We have measured the mechanical properties of the Si and silicon nitride films used to produce shutters and shutter arrays. Using these properties, we have modeled the performance of actual microshutters, and have found excellent agreement between model and experiment. Thus the modeling can be an important design tool in the production of large arrays, and will be critical in estimating the overall relability of arrays given the statistics of defects in the materials.

The operating temperature of the micro-shutter array will be 30K. The thermally induced mismatch stresses between the membrane and coating is not expected to result in failure because the coatings are thin. Particular care must be taken to avoid thermal mismatches between the arrays and the packaging. For final validaton, strength and stiffness of representative samples must be measured at 30 K to provide definitive estimates of mechanical performance.

2.4.3 Single Shutter Actuation

Having developed a reliable shutter, we fabricated and tested our actuation mechanism,the doubleshutter. First tests were carried out with single shutter pair to demonstrate the selection concept.

The shutters were brought in close contact, engaged by applying DC voltage, then moved to "open" position, when the shutter was perpendicular to the membrane plane, and then disengaged. Although all tests have been carried out at room temperature, there are no factors that would prevent these shutters from operating at cryogenic temperatures. Currently we are in the process of fabricating and testing small 2D-arrays of shutters (typical size 5 by 5 elements).

These tests also demonstrated that mechanical design tolerates significant lateral motions during actuation. The required tolerances on the actuator are 2-3 μm .

2.4.4 Actuation Schemes And Shutter Arrays

We consider two different actuator designs for the doubleshutter 2.2.

- The actuator array is mounted on a 2 - d stage with piezoelectric actuators. A computer controller provides motion relative to the second (fixed) array along the required quarter circle (quadrant) to open the shutters.
- The actuator array is mounted to the fixed array on a four bar linkage which constrains the motion along the required quadrant. The motion along the circle is generated by a 1 - d stage.

At this time we consider the doubleshutter actuation mechanism as the preferred solution. There are other possible designs that deserve consideration for further alternative developments.

- Single shutters could be selected using resonant excitation with an array of additional electrodes for electostatic locking mounted perpendicular to the array plane[23].
- shutters in a single array (as opposed to the doubleshutter array) can be selected using an e-beam excitation. The e-beam steering equipment of a TV tube could be used to address an array. This concept appeared when a highly resistive silicon nitride shutter flipped over by 180°when illuminated with the electron beam in an electron microscope. It has the advantage of simplicity compared to the doubleshutter.

2.5 Transition To Production Technology

Having demonstrated the microshutter concept on a small scale, the next step in the development is the production of larger arrays. Focused ion beam milling is not a useful tool for such arrays because it takes too long to machine them. However, the arrays can be machined rapidly using photolithographic processing. This process consists of two independent, but compatible elements:

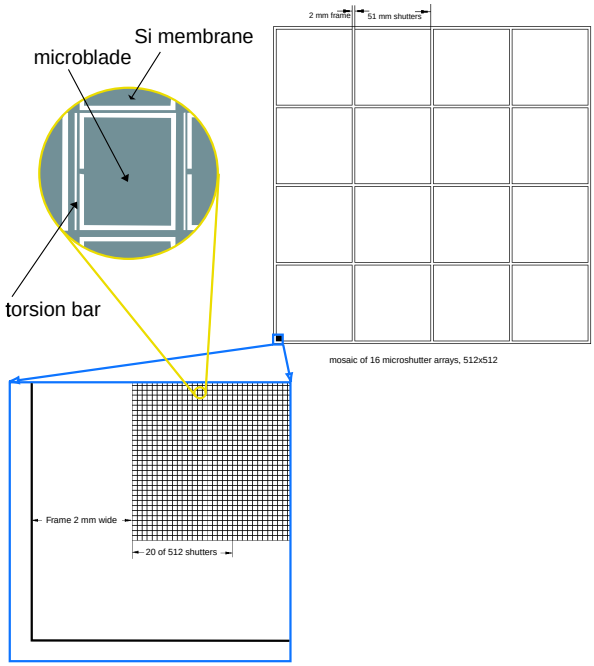

Figure 2.7: Layout of the 2048 by 2048 microshutter array. 512 by 512 shutter arrays are arranged in mosaic on a frame with 2 mm thick ribs. Expanded views shows the corner of the mosaic and single microshutter.

A CMOS process to create the addressing circuitry on the actuator array and a process to create the mechanical structures on both the shutter and actuator array. Both of these process are currently in use in the GSFC Detector Development Lab (DDL). The CMOS process is a standard for transistor fabrication. The micromechanical structures can be fabricated using the process developed for pop-up detectors.

The devices will be fabricated using a starting substrate 100 micrometer thick, 4 inch silicon base wafer. There are two layers on the substrate, an etch stop directly on the wafer and the active shutter layer on that. The required address circuitry will be processed first using the standard CMOS process. The major challenge for our application lies primarily in the definition of the device geometry. The selection transistors must be small enough to fit on the 10μm wide frame which supports the microshutters. The row and column select electronics must be mounted on two perpendicular sides of the array.

The Pop-up bolometer process developed in the DDL includes all necessary steps for the production of the mechanical structures. At this time we anticipate a two step process: a Deep Reactive Ion Etching (Deep RIE) step which anistropically structures the base wafer and forms the support structure (10 micron wide, 100 micron tall) to carry both the shutters and the address circuitry and a single RIE process which patterns the remaining membrane into shutters.

Layouts and process recipes will be tested first on small arrays (32x32). After such arrays have worked successfully, the processes will scaled up to a final size of 512x512. To produce even larger arrays, a mosaicing process will be developed, where arrays of 512x512 shutters are put together to form larger units 2.7. The mosaicing has the disadvantage of requiring additional support structures. The important advantages the mosaicing are the facts that the the mosaic structure can be developed in parallel with the arrays and that the 512x512 mosaic modules can be produced and analyzed with tested equipment once the process is established, independent of the size of the mosaic.

2.6 Technology Readiness

We assessed the Technology Readiness Level(TRL) of a MOS instrument based on a transmissive microshutter as of today (table 2.6.1) and as it should be by instrument selection in April 2001 (table 2.6.3). We assumed that development proceeds as planned in section 2.6.2. This assessment is based upon the nine chart "TRL Determination" taxonomy in current use at NASA. The taxonomy itself is the product of systems research based upon the history of advanced instrument development. In this taxonomy, a TRL of 1 indicates a low readiness level and a TRL of 9 indicates a very high degree of readiness.

The transmissive microshutter development effort has received or will receive funds from NGST Technology Development, NASA Headquarters Cross–cutting Technology Development and the Explorer Program Technology development, as shown in table 2.6.

Source	**Amount(k$)**	**When Available**
NGST Technology	75	June 1998
HQRS Cross–cutting	267	September 1999
Explorer Technology	235	September 1999

Table 2.1: Funds available for transmissive microshutter development as of September 1999.

We will submit a proposal to continue development of the transmissive microshutter in response to the upcoming NGST Technology Development AO.

2.6.1 Current Status

The current status of transmissive microshutter development, discussed extensively in section 2.3, is briefly summarized below;

- Identified the optical requirements.
- Developed a single shutter concept design, selected materials.

- Developed an FEM model of the concept design, analyzed the concept design and based upon the results, optimized the design.
- Identified a fabrication method suitable for prototype shutter arrays: an FEI 620 focussed ion beam milling machine.
- Fabricated a single shutter prototype and by testing determined fundamental mechanical properties and stress failure modes.
- Identified photo-lithography as the appropriate fabrication method for large arrays.
- Developed a doubleshutter actuation scheme for a 2D shutter array.
- Fabricated a 5×5 microshutter having a 3×3 portion configured as a doubleshutter, addressable and actuatable; tested actuation approach and fundamental mechanical properties.
- Identified several ways to electronically stimulate shutter actuation.

Our rather conservative assessment of the TRL level of a MOS instrument using a transmissive microshutter array is shown in table 2.6.1. It is not clear what form the MOS instrument will take at this time. However, our team has a wealth of experience, in the lab and in orbit, with the components and sub-systems that will make up the MOS spectrograph. We are experienced at cryogenic instrument techniques(e.g. DIRBE on COBE, SIRTF on IRAC). Successful development and deployment of a MOS instrument on NGST appears very feasible.

2.6.2 Development Plan

To develop the transmissive microshutter, the following additional tasks must be performed:

1. Design and fabricate a 128×128 array with a ground plane simulating a doubleshutter using photolithographic process; perform mechanical characterization and life testing.
    - Design and fabricate a second 128×128 array with a 32×32 doubleshutter portion that is addressable.
2. Design and fabricate a 512×512 array with a ground plane simulating a doubleshutter; perform mechanical characterization and life testing.
3. Design and fabricate 512×512 doubleshutter array, fully addressable and actuatable with on-array electronics.
4. Optical performance and characterization of 512×512 doubleshutter array.
5. Qualification testing of 512×512 doubleshutter array.

- Thermal (properties, differential induced stress)
- Vibration(Random, Sine, Shock, Acoustic)
- Radiation
  - SEU
  - Total dose
- Contamination effects(in vacuum, while operating)
  - Sticktion

6. Post-environmental optical performance and characterization testing of 512×512 doubleshutter array.
7. Design micro-machined kinematic mounts and mosaic frame for 4×4 mosaic of 512×512 microshutter arrays.
8. Design and fabricate prototype 1024×1024 doubleshutter microshutter array (mosaic of 4 512×512 doubleshutter arrays) and actuation electronics testbed.
9. Optical performance and characterization of 1024×1024 doubleshutter array.
10. Qualification testing of 1024×1024 doubleshutter array mosaic(see above for details).
11. Post-environmental optical performance and characterization testing of 1024×1024 doubleshutter array.
12. Modify design and re-test as required.
13. Design and fabricate MOS engineering model microshutter array(2048×4096) and EM actuation electronics.
14. Perform environmental qualification testing as required.

Our plan is to fund two development teams. One team will concentrate on the mechanics of the photolithographic process to form microshutters. The other team will concentrate on the design and lay–down of microelectronics on the microshutter to control and actuate. Both teams will first concentrate on the process design, and then, and scaling up to full size 512×512 arrays. Specialists in parts quality assurance are already involved to ensure that our design leads, in an evolutionary way, to a flight qualifiable component. Specialists in optical metrology will be involved to provide an independent assessment of the optical characteristics and performance of the flight–like microshutter prototypes. The entire development plan is designed to support a MOS instrument development for NGST at the lowest possible risk.

2.6.3 Readiness By Instrument Selection

By instrument selection(April 2001), we will have completed the following:

- A working prototype 128×128 array for mechanical and life test.
- A prototype 512×512 microshutter array for mechanical test.
- Test results characterizing the performance, mechanical properties, and ability to withstand launch loads.
- A process for developing large scale(512×512) microshutter arrays.
- A 512×512 doubleshutter array with lab electronics to support testing.
- Optical performance and characterization test results for the 512×512 doubleshutter array.

We believe the technology readiness concern with the microshutter array will be substantially abated by the time instruments are selected. Our assessment of the TRL level of a transmissive microshutter based MOS is shown in table 2.6.3. We will have a working flight–like prototype array under test and a MOS instrument design proceeding into phase A/B. To complete development, tasks 5 thru 14, post-selection funding will be required with development completed by CDR.

After completion of the transmissive microshutter development plan, MOS instrument development should proceed normally.

2.7 Development Schedule and I & T

2.7.1 Microshutter Development Schedule

The transmissive microshutter development schedule is shown in figure 2.8. Only the development of the transmissive microshutter component is depicted.

Microshutter Specific I & T Issues

The following issues must be addressed during assembly, integration and test verification of a transmissive microshutter based MOS instrument:

1. Cryogenic operation only, close to thermal equilibrium.
2. Contamination susceptibility; control procedures.
3. Optical performance characterization.
4. Lifetime; shutter cycles.

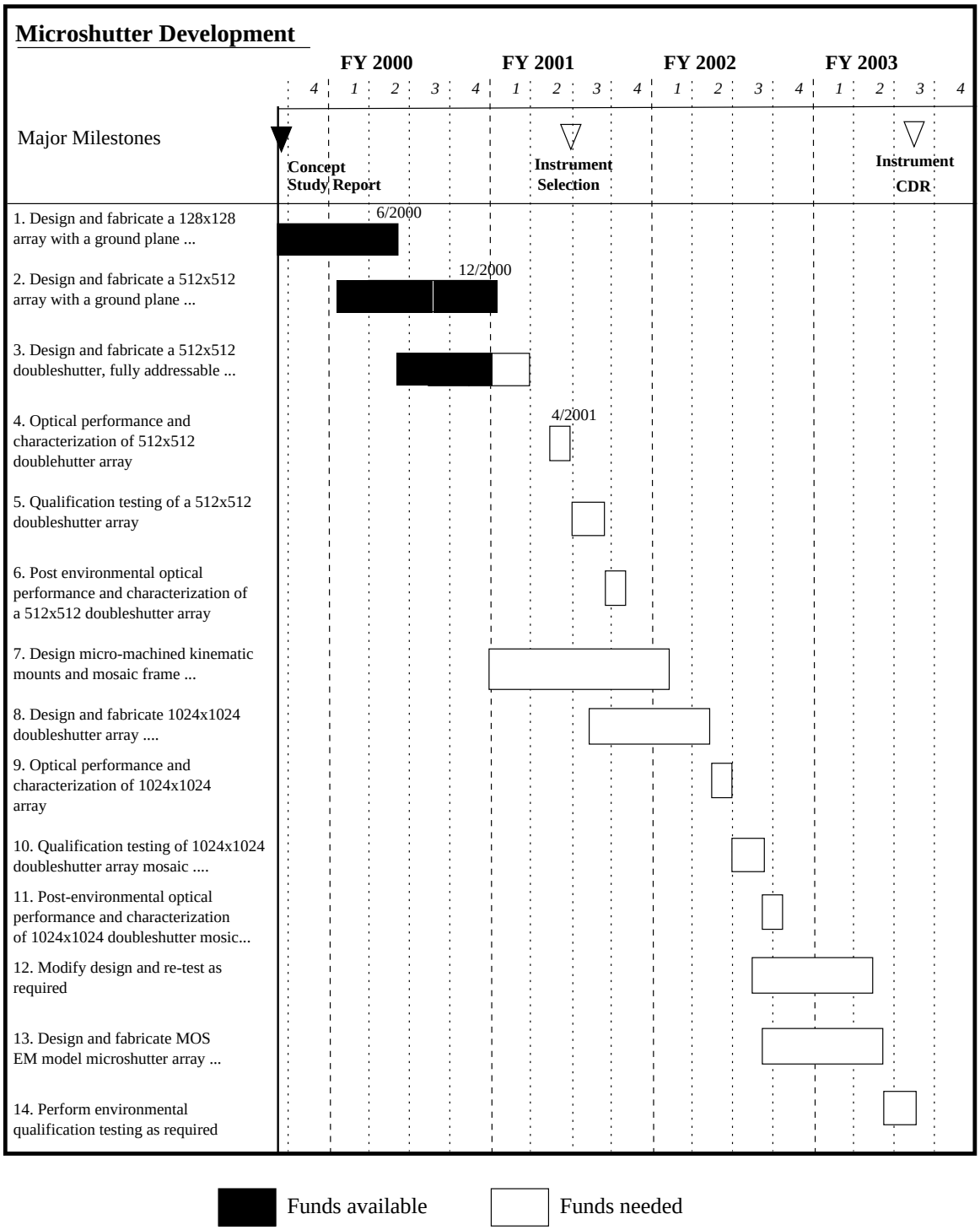

Figure 2.8: Development schedule for the transmissive microshutter array component. Tasks are identified in section 2.6.2.

5. Alignment
    - Between layers of the doubleshutter
    - To frame of mosaic
    - Thermal stability-hysteresis

The Assembly, Integration and Test verification flow the transmissive microshutter component is shown in figure 2.9.

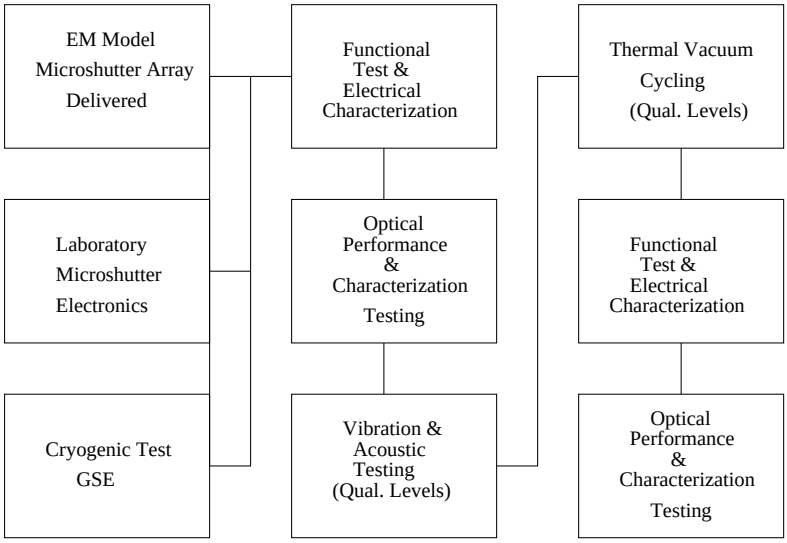

Figure 2.9: Flight qualification of a transmissive microshutter array for an MOS instrument. All testing will be performed at cryogenic temperatures.

Chart 2: Proposed Instrument Based on Research Studies–No Previous Flight Experience for Proposed Instrument		
• Have analytical & experimental studies been concluded that demonstrate viability of critical functions and provide proof of concept?	Yes	
• Have an integrated Phase A study been completed?	No	TRL=2.5
Chart 7: TRL Adjustments for PI Experience and Technical Complexity		
• Is this at least the 2nd instrument development for the PI?	Yes	
• Is proposed inst. same inst. family as PI's previous instrument?	Yes	TRL +.5
• What is the level of detector cooling required?	2-90 deg K	TRL - .25
Chart 8: TRL Adjustments for Mission Criticality and Ease of Fall-Back Position		
• Will the proposed instrument account for 50% or more of the mission science or 35% or more of the total payload cast?	No	No TRL Change
• Can the proposed instrument be descoped by 20% or more if needed without impacting Level 1 Science Requirements?	Yes, reduced perf.	No TRL Change
Chart 9: TRL Adjustments for Instrument Family Maturation		
• If the proposed instrument is categorized as:	Spectrometer	TRL + .5

Table 2.2: As of September 1, 1999, a MOS based on transmissive microshutter technology has a TRL of 3.25.

Chart 1: Guide to Initial TRL Determination(Before Adjustments) for Proposed Instrument		
• Proposed Instrument is Based on Prior Hardware/Software Developments and/or Flight experience		
• There are validated components and/or breadboards either in lab or some flights	Yes	Chart 3
Chart 3: Proposed Instrument Has Validated Components and/or Breadboards		
• Have components/breadboards been validated by orbital flight?	Yes	
• 50% of key components/breadboards validated in orbital flight?	Yes	
• PI can commit to firm margins & schedule?	Yes	TRL=5
Chart 7: TRL Adjustments for PI Experience and Technical Complexity		
• Is this at least the 2nd instrument development for the PI?	Yes	
• Is proposed inst. same inst. family as PI's previous instrument?	Yes	TRL +.5
• What is the level of detector cooling required?	2-90 deg K	TRL-.25
Chart 8: TRL Adjustments for Mission Criticality and Ease of Fall-Back Position		
• Will the proposed instrument account for 50% or more of the mission science or 35% or more of the total payload cast?	No	No TRL Change
• Can the proposed instrument be descoped by 20% or more if needed without impacting Level 1 Science Requirements?	Yes, reduced perf.	No TRL Change
Chart 9: TRL Adjustments for Instrument Family Maturation		
• If the proposed instrument is categorized as:	Spectrometer	TRL + .5

Table 2.3: Following completion of the development plan outlined in section 2.6.2, the TRL level for a transmissive microshutter based MOS at instrument selection(April 2001) should be 5.75.

Chapter 3

Cost Estimate

3.1 Cost Summary

This cost estimate is for technology development of the transmissive microshutter only and is based upon the development tasks identified in section 2.6.2. We assume that phase A/B begins immediately after instrument selection and that phase C begins immediately following CDR. Microshutter development should be complete by CDR. Normal instrument development costs are not included; however, some of the cost an engineering model for a MOS instrument is included. Costing reflects the development schedule shown in figure 2.8. Full cost accounting is assumed with labor costs in current year dollars. This is a ROM estimate only for a hypothetical MOS instrument development.

The transmissive microshutter development effort has received or will receive funds from NGST Technology Development, NASA Headquarters Cross–cutting Technology Development and the Explorer Program Technology development, as shown in table 2.6.

3.2 Details

3.2.1 Management

Includes procurement and sub-contract management until instrument selection. We assume that these costs fall under the instrument development project after selection.

3.2.2 Science Program Development

Includes resolution of scientific issues; MOS instrument performance analysis; performance requirements analysis; mission impact evaluations; and analysis of microshutter test data.

WBS	<A			A/B			C/D			
	CS	Cont	Mat.	CS	Cont	Mat.	CS	Cont	Mat.	
	K$	*K$*	*K$*	*K$*	*K$*	*K$*	*K$*	*K$*	*K$*	*Sub−total*
1.0 Management	26.7	0.0	0.0	1.4	0.0	0.0	0.0	0.0	0.0	28.1
2.0 Science program development	142.6	0.0	0.0	105.1	0.0	0.0	0.0	0.0	0.0	247.7
3.0 Systems Engineering	15.8	0.0	0.0	0.8	0.0	0.0	0.0	0.0	0.0	16.6
4.0 SR&QA	12.5	53.7	0.0	17.4	109.6	0.0	0.0	0.0	0.0	193.2
5.0 Structure	58.7	50.4	0.0	139.1	111.9	0.0	0.0	0.0	0.0	360.1
6.0 Optics	213.1	133.5	144.0	119.2	233.6	76.0	0.0	0.0	0.0	919.4
7.0 Electronics	0.0	0.0	0.0	52.5	36.7	30.0	0.0	0.0	0.0	119.3
8.0 Thermal Engineering	0.0	6.3	0.0	0.0	10.0	0.0	0.0	0.8	0.0	17.1
9.0 Software	0.0	8.4	50.0	0.0	55.9	30.0	0.0	0.0	0.0	144.3
10.0 Detectors	0.0	0.0	0.0	0.0	0.0	0.0	0.0	0.0	0.0	0.0
Sub−total	469.3	252.2	194.0	435.6	557.8	136.0	0.0	0.8	0.0	2045.7

Figure 3.1: Estimated cost to develop a transmissive microshutter array for a MOS instrument.

3.2.3 Systems Engineering

Includes requirements identification and tracking, report generation and general support until instrument selection. We assume that these costs fall under the instrument development project after selection.

3.2.4 SR&QA

Includes support concentrating on materials analysis, failure analysis and parts qualification, extending until the end of FY02 when these costs will fall under instrument development.

3.2.5 Structure

Extensive effort to develop micro machined kinematic mounts, alignment procedures, and a frame for the 1024x1024 mosaic frame, and the MOS EM frame. This line also includes mechanical analysis; mechanism design; and fatigue analysis.

3.2.6 Optics

Includes design and fabrication of the microshutter arrays; materials needed to fabricate the arrays; development of the on–array electronics; cryogenic testing; optical metrology; and qualification testing. Sub-contracts to universities and other labs are under this line.

3.2.7 Electronics

Includes support for the design and fabrication of electronics for the actuator testbed.

3.2.8 Thermal Engineering

Includes thermal and contamination discipline support for the design, fabrication and qualification testing of the microshutter array.

3.2.9 Software

Includes software development and off–the–shelf equipment needed for actuator testbed.

3.2.10 Detectors

Not applicable.

Appendix A

A Comparison of the Prism Mode with Multi-Filter Imaging

A.1 Motivation

Low resolution ($R \lesssim 40$) observations of galaxy spectral energy distributions (SED's) give us the opportunity to use the highly successful photometric redshift method (see [35] for a review) to determine redshifts for every object selected by the multi-shutters. The current state of the art in photometric redshifts routinely produces estimates good to 5% of redshift [10]. Our prism mode provides simultaneous observations of the full $0.6 - 5\mu$m spectral range with the resolution of medium-band filters to accomplish prime NGST science objectives efficiently.

To investigate the utility and implementation issues of the prism mode, we carried out Monte-Carlo simulations of photometric redshifts from model SED's. For the sake of redshift estimation, we treat the prism mode as a series individual resolution elements, much like a filter set. This allows us to make direct comparison between camera-mode medium-band filter observations and prism spectra.

A.2 Photometric Redshifts

The concept of photometric redshifts has been explained in detail in the many papers which have sucessfully applied it to catalogs of galaxy photometry [36, 37, 38, 39, 40, 41], Briefly, the SED of a candidate galaxy is compared to a database of template spectra at all redshifts; the best fit between the two is considered to be the photometric redshift. Although the idea is simple, it relies on the complicated question of choosing the proper template spectra.

Remarkably good results ($\sigma_z/z \sim 0.05$) are obtained out to redshifts $z \sim 6$ with only a handful of observed low-z templates ([39] using the spectra of [42]) or with a standard set of spectral synthesis models ([40] using the GISSEL98 models of [43]). The errors in inferred redshift result from a

combination of photometric uncertainty and the intrinsic difference between observed galaxies and the template SEDs. However, better accuracy appears possible by fitting the integrated colors of empirical spectra at the redshifts and galaxy types of interest [37]. In the best case, this method eliminates the uncertainty resulting from inappropriate templates. The empirical-fitting method requires a large database of measured spectra over all redshifts, but such data would likely be available from the first deep fields with NGST. For our simulations, we have assumed that the empirical-fitting method is a viable option, and have chosen to model the recovery of redshifts using the same input and output model templates.

Specifically, for our template set we have used GISSEL96 [43] spectral synthesis models, covering 0.5-20 Gyr ages, with solar or lower metallicty and Salpeter IMF's. The templates are convolved with the filter or prism response and noise is added. The data and models are then compared at each resolution element. Following typical photometric redshift techniques, we perform χ^2 tests on a suite of redshifted template spectra. The inferred redshift is the one with the lowest χ^2 value.

A.3 Simulations

To produce our simulated galaxy observations, we must assume a redshift distribution and an apparent magnitude distribution. We take our redshift distribution from the photometric redshifts of [10] for the Hubble Deep Field North (HDF-N; [2]). Since spectroscopy of HDF-N galaxies is currently limited to $z < 6$, we extrapolate the distribution by assuming a flat number-redshift relation from $6 < z < 15$ (see figure A.1).

The flux distribution of the simulated galaxies (see figure A.2) is determined from the number-magnitude relation of the STIS observations of the HDF-South [5]. Those number counts are shifted to the K-band using a model of the median galaxy colors [7]. The apparent magnitude distribution is sampled independently of the redshift distribution, but extremely unlikely luminosities are eliminated ($L > 10L_*$ or $L < 0.01L_*$).

For comparison with camera-mode observations, we assume a logarithmically spaced set of filter wavelengths and widths, covering the $1-5\mu$m range. Photometric errors for filter observations were calculated using a signal-to-noise estimator consistent with the ISIM Yardstick camera specifications [44]. Table A.1 lists the parameters assumed.

Zodi model	Stiavelli 1998 [45]
Dark Current	$0.02e^-$/sec/pixel
Read Noise	$4e^-$ rms
QE	80%
Diffraction Limit	2μm

Table A.1: Assumed properties in signal-to-noise calculations from the NGST Yardstick ISIM study [44].

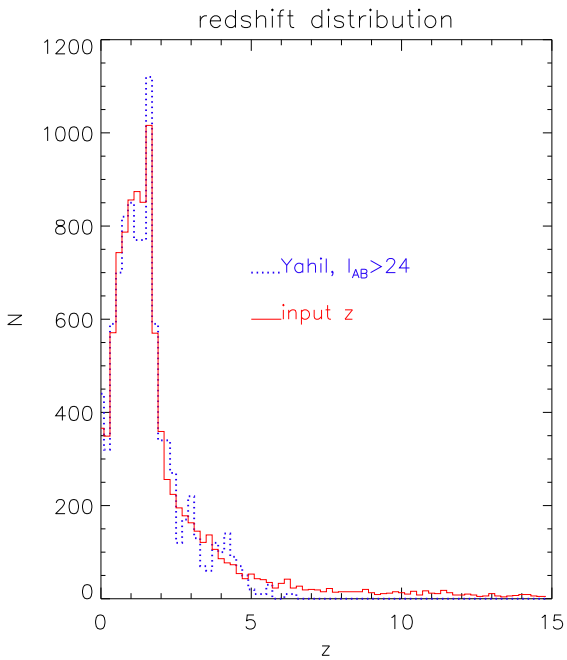

Figure A.1: The redshift distribution of simulated galaxies, compared to the distribution of photometric redshifts of faint galaxies in the HDF-N compiled by Yahil et al. 1999.

In the medium-band case of diffraction limited observing, the sensitivity of serial observations scales with resolution. That is, for fixed total observing time for all filters, signal-to-noise is decreased by the square root of the time per filter *and* by the square root of the decrease in signal from the narrower filter.

The prism-mode sensitivity is a function of the varying resolution across the wavelength range, in addition to the zodiacal light and detector noise characteristics. Manufacturing limitations may prevent a constant resolution across $1-5\mu$m, with a worst case shown in figure A.3. Further study of prism properties will produce a more optimal prism.

A.4 Optimal Resolutions

We first investigated the question: what is the optimal resolution for medium-band filters to obtain photometric redshifts. We ran Monte Carlo simulations for a series of filter resolutions with a fixed total integration time of 10^5 seconds. Figure A.4 shows that averaged over all redshifts, 40 filters produce the most accurate photometric redshift estimates for galaxies with reasonable signal-to-noise per resolution element.

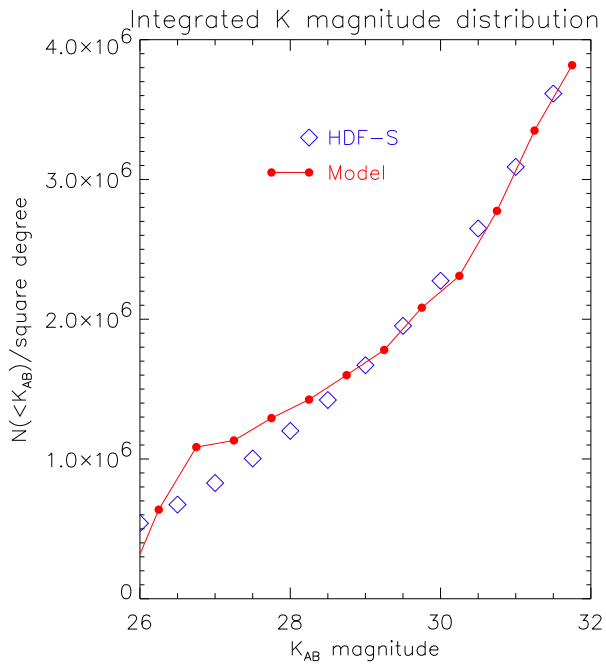

Figure A.2: The number-magnitude relation of simulated galaxies, compared to the number counts of galaxies in the HDF-S compiled by Gardner et al. 1999

A.5 Advantage of a Prism

For a single object, the advantage of a prism over medium-band filters is clear – it measures the entire wavelength range simultaneously. Integration time per filter goes down as resolution for serial observations. So at first glance, one might expect an advantage for the prism equal to the square root of the resolution. An ideal $R = 25$ prism might recover redshifts $\sqrt{25} = 5$ times more efficiently than filters. In reality, the varying prism resolution across the wavelength range would decrease this advantage. Figure A.5 shows the advantage of prism observations over filter observations for a magnitude limited sample.

Put another way, prism observations will reach fainter galaxies in the same observing time and resolution for a fixed σ_z. They will also recover a more complete sample of redshifts (depending on constraints of multi-shutter selection). Figures A.6 - A.8 detail these advantages. In 10^5 seconds, filter observations recover less than 50% of measured galaxies at $K_{AB} > 30$. Even the worst-case prism, however, recovers galaxies a magnitude fainter. It is at magnitudes fainter than 30 that NGST will make the most revolutionary discoveries.

The prism's ability to accomplish the core science goals also depends on the number of targets that can be measured in each mode, as well as the accuracy of the recovered redshifts. Since prism spectra will take up only a fraction of the pixels available in each row, the low resolution mode

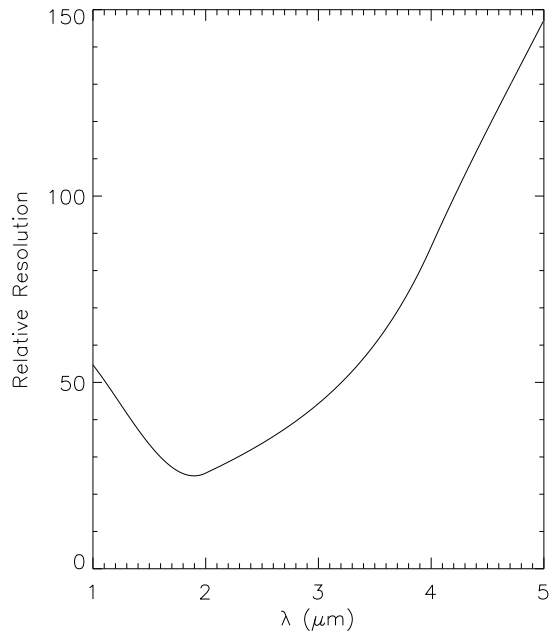

Figure A.3: The resolution as a function of wavelength for the near-IR prism. The minimum resolution can be selected to meet science goals; this figure shows the resolution of the nominal prism, but the mininum value (where R=25 on this figure) could be changed, without changing the relative shape of the plot.

will have a high degree of completeness at the magnitudes of interest (see the discussion in Section 1.2.2).

A.6 Conclusions

Low resolution prism observations of galaxy SED's provide a significant advantage over multi-filter observations for any realistic observing strategy. For an ideal prism in background limited observing, the prism has a signal-to-noise advantage of square root of the resolution over serial observations by filters with similar resolution. This added depth reaches at least a magnitude fainter in recovery of photometric redshifts with the prism over filter observations at *any* resolving power. Extensive simulations suggest that in 10^5 seconds an ideal prism will recover the redshift of 80% of measured objects (subject to MOS selection) down to $K_{AB} = 32$, with an accuracy of $\delta_z < 3\%$, compared to less than 40% of the objects with serial filter observations.

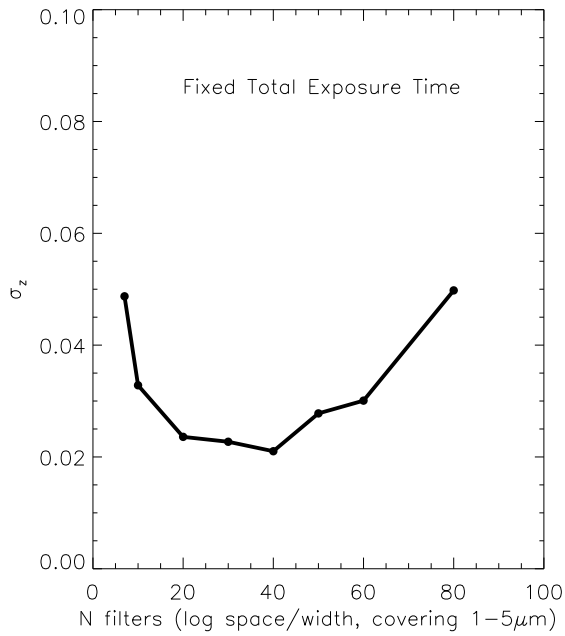

Figure A.4: The deviation in recovered redshifts from the input as a function of resolution (number of filters). The total exposure time is fixed at 10^5 seconds. The sample is magnitude limited to $K_{AB} < 29.5$, where SNR=10 at 2.2μm for the 40-filters resolution. Catastrophic failures were excluded from the statistics. Filters have wavelength centers and widths evenly stepped in log(λ). Simulated galaxies were selected from the redshift distribution shown in figure A.1

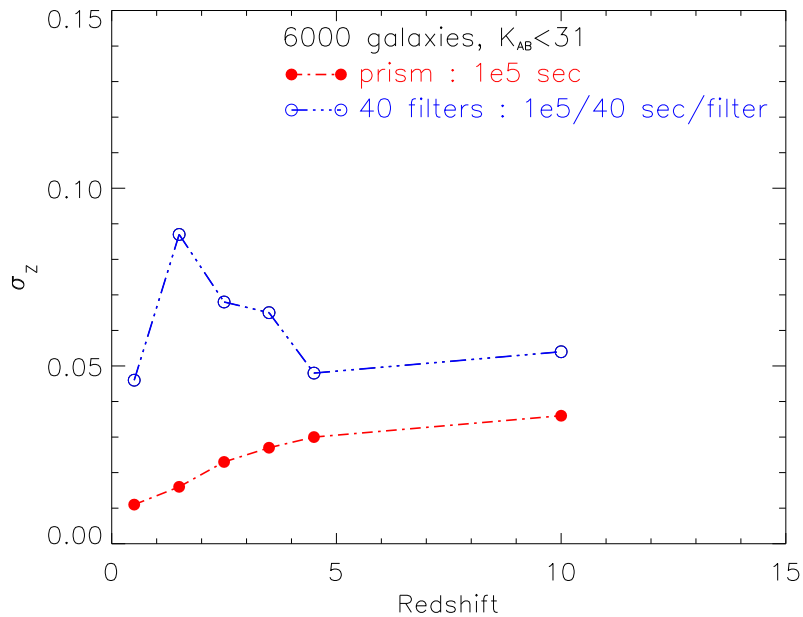

Figure A.5: The deviation in recovered redshifts from the input as a function of redshift. The total exposure time is fixed at 10^5 seconds. The sample is magnitude limited to $K_{AB} < 31$, where SNR=10 at 2.2μm for the worst case prism resolution. Catastrophic failures in redshift recovery ($\delta_z > \frac{z}{2}$) are not included in the calculation of σ_z, so the prism has an addition advantage not shown here to recover a larger percentage of observed galaxies. The worst bin for σ_z with the filters is $1 < z < 2$ where the 4000Å break is not always well measured. The higher SNR for the prism compensates for this problem.

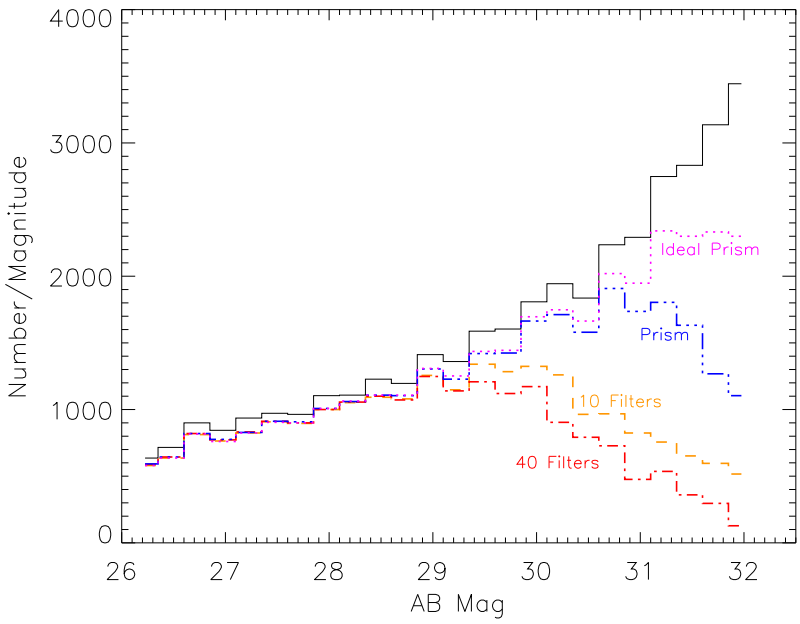

Figure A.6: Histogram of the fraction of recovered redshifts. From a sample of 10,000 simulated galaxies (all assumed to be measured by both prism and filters), the histogram shows the fraction recovered with $\delta_z < 3\%$.

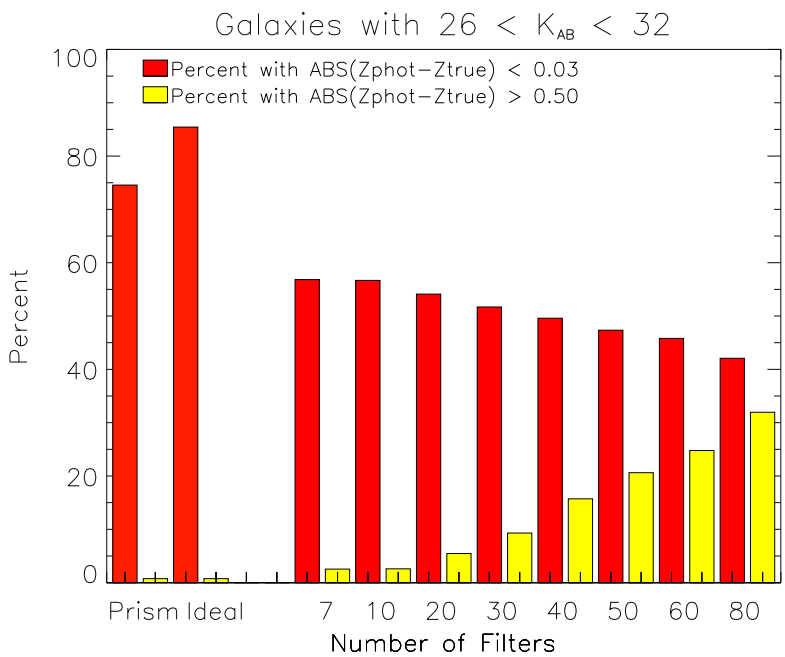

Figure A.7: Percentage of recovered redshifts. From a sample of 10,000 simulated galaxies with $K_{AB} < 32$ (all assumed to be measured by both prism and filters in 10^5 seconds total exposure time), the fraction recovered with $\delta_z < 3\%$ is plotted as a function of filter resolution. Also plotted is the percentage of catastrophic failures.

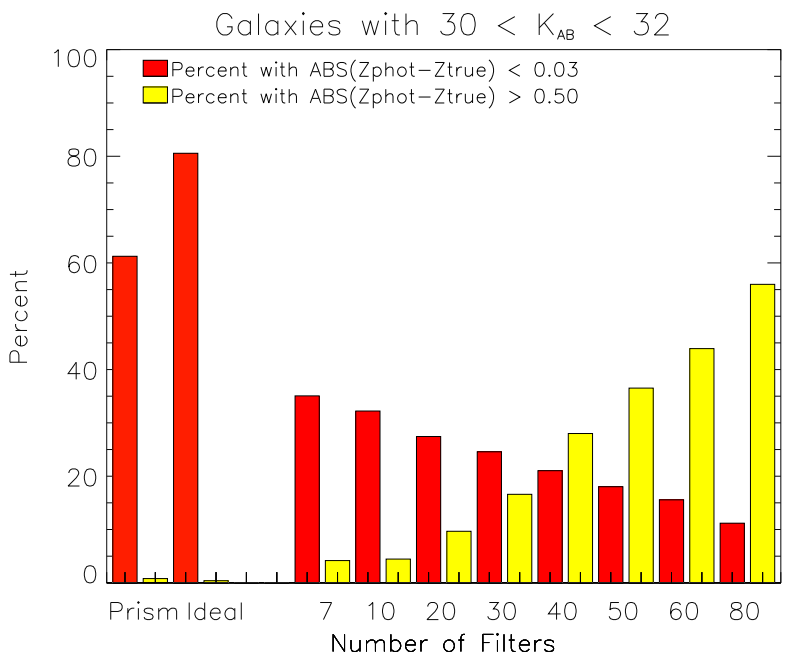

Figure A.8: Percentage of recovered redshifts. From the faint end ($30 < K_{AB} < 32$) simulated galaxy distribution in figure A.7 the fraction recovered with $\delta_z < 3\%$ is plotted as a function of filter resolution. Also plotted is the percentage of catastrophic failures.

Bibliography

[1] H. S. Stockman. *Next Generation Space Telescope, Visiting a Time When Galaxies Were Young*. 1997.

[2] R. E. Williams, B. Blacker, M. Dickinson, W. V. D. Dixon, H. C. Ferguson, A. S. Fruchter, M. Giavalisco, R. L. Gilliland, I. Heyer, R. Katsanis, Z. Levay, R. A. Lucas, D. B. MCElroy, L. Petro, M. Postman, H. M. Adorf, and R. Hook. The Hubble Deep Field: Observations, data reduction, and galaxy photometry. *AJ*, 112:1335+, October 1996.

[3] R. E. et al. Williams. The Southern Hubble Deep Field. *AJ, in prepation*, 1999.

[4] R.I. Thompson, L.J. Storrie-Lombardi, R.J. Weymann, M.J. Rieke, G. Schneider, E. Stobie, and D. Lytle. NICMOS observations of the Hubble Deep Field: Observations, data reduction, and galaxy photometry. *AJ, in press, astro-ph/9810285*, 1999.

[5] J. P. Gardner and et al. The hubble deep field south: Stis imaging. *AJ, submitted*, 1999.

[6] J. P. Gardner and S. Satyapal. Galaxy count and sizes in the Hubble Deep Field South. *in preparation*, 1999.

[7] J. P. Gardner. An extendable galaxy number count model. *PASP*, 110:291–305, March 1998.

[8] H.I. Teplitz, I.S. McLean, E.E. Becklin, D.F. Figer, A.M. Gilbert, J.G. Graham, J.E. Larkin, N.A. Levenson, and M.K. Wilcox. The rest-frame optical spectrum of MS1512-cB58. *ApJ, in preparation*, 1999.

[9] M. Pettini, M. Kellogg, C. C. Steidel, M. Dickinson, K. L. Adelberger, and M. Giavalisco. Infrared observations of nebular emission lines from galaxies at $z \sim 3$. *ApJ*, 508:539–550, December 1998.

[10] A. Fernandez-Soto, K. M. Lanzetta, and A. Yahil. A new catalog of photometric redshifts in the Hubble Deep Field. *ApJ*, 513:34–50, March 1999.

[11] P. Madau, H. C. Ferguson, M. E. Dickinson, M. Giavalisco, C. C. Steidel, and A. Fruchter. High-redshift galaxies in the Hubble Deep Field: colour selection and star formation history to $z \sim 4$. *MNRAS*, 283:1388–1404, December 1996.

[12] C. C. Steidel, M. Giavalisco, M. Dickinson, and K. L. Adelberger. Spectroscopy of Lyman break galaxies in the Hubble Deep Field. *AJ*, 112:352+, August 1996.

[13] J. D. Lowenthal, D. C. Koo, R. Guzman, J. Gallego, A. C. Phillips, S. M. Faber, N. P. Vogt, G. D. Illingworth, and C. Gronwall. Keck spectroscopy of redshift z approximately 3 galaxies in the Hubble Deep Field. *ApJ*, 481:673+, May 1997.

[14] H.S. Stockman, D. Fixsen, R. Hanisch, J.C. Mather, M. Nieto-Santisteban, J.D. Offenberg, R. Sengupta, and S. Stallcup. Cosmic ray rejection and image processing aboard the Next Generation Space Telescope. In *NGST Workshop, in press*, 1999.

[15] J.D. Offenberg, R. Sengupta, D. Fixsen, H.S. Stockman, M. Nieto-Santisteban, S. Stallcup, R. Hanisch, and J.C. Mather. Cosmic ray rejection with NGST. In D.M. Mehringer, R.L. Plante, and D.A. Roberts, editors, *Astronomical Data Analysis Software and Systems VIII*, volume 172, page 141, 1999.

[16] J.D. Offenberg. *private communication*, 513:34–50, March 1999.

[17] H.S. Stockman. *The Next Generation Space Telescope: visiting a time when galaxies were young*. The Association of Universities for Research in Astronomy, Inc., 1997.

[18] J.W. MacKenty and M. Stiavelli. A multi-object spectrometer using micro mirror arrays. In W. van Breugel and J. Bland-Hawthorn, editors, *IMAGING THE UNIVERSE IN THREE DIMENSIONS: Astrophysics With Advanced Multi-Wavelength Imaging Devices*, 1999.

[19] E. J. Garcia, M. A. Greenhouse, B. Mott, and J. L. Kuhn. Surface micromachined micromirror arrays for the next generation space telescope. *American Astronomical Society Meeting*, 194:9107, May 1999.

[20] S.H. Moseley et al. Programmable 2-dimensional microshutter array. *ASP Conference Series*, 1999.

[21] R. Fettig, S.H. Moseley, A.S. Kutyrev, J. Orloff, J.L. Kuhn, and L Shude. Some aspects on the mechanical analysis of micro-shutters. In *Materials and Device Characterization in Micromachining II*, volume 3875, 1999.

[22] E.J. Garcia. Micro-flex mirror and instability actuation technique. In *Proceedings of IEEE the* 11th *Annual International Workshop on Micro Electro Mechanical Systems*, pages 470–475, 1998.

[23] K. Yamada and T. Kuriyama. A novel asymmetric silicon micro-mirror for optical beam scanning display. In *Proceedings of IEEE the* 11th *Annual International Workshop on Micro Electro Mechanical Systems*, pages 110–115, 1998.

[24] J. Kränert, C. Deter, T. Gessner, and Dötzel. Laser display technology. In *Proceedings of IEEE the* 11th *Annual International Workshop on Micro Electro Mechanical Systems*, pages 99–104, 1998.

[25] Jan-Ake Schweitz and Fredric Ericson. Evaluation of mechanical materials properties by means of surface micromachined structures. *Sensors and Actuators*, 74:126–133, 1999.

[26] W.A. Weibull. A statistical distribution function of wide applicability. *J. Appl. Mech.*, 18:293, 1951.

[27] Fredric Ericson and Jan-Ake Schweitz. Micromechanical fracture strength of silicon. *J. Appl. Phys.*, 68(11):5840–5844, September 1990.

[28] C.J. Wilson, A. Ormeggi, and M. Narbutovskih. Fracture testing of silicon microcantilever beams. *J. Appl. Phys.*, 79(5):2386–2393, March 1996.

[29] Stefan Johansson and Jan-Ake Schweitz. Fracture testing of silicon microelements in situ in a scanning electron microscope. *J. Appl. Phys.*, 63(10):4799–4803, May 1988.

[30] Walter D. Pilkey. *Formulas for stress, strain, and structural matrices*. J. Wiley, New York, 1994.

[31] Warren C. Young. *Roark's Formulas for Stress and Strain*. McGraw-Hill, Inc., New York, 1989.

[32] B Bhushan and X.D. Li. Micromechanical and tribological characterization of doped single-crystal silicon and polysilicon films for microelectromechanical systems. *J. Mater. Res.*, 12(1):54–63, January 1997.

[33] N.C. MacDonald, L.Y. Chen, J.J. Yao, Z.L. Zhang, J.A. McMillan, D.C. Thomas, and K.R. Haselton. Selective chemical vapor-deposition of tungsten for microelectromechanical structures. *Sensors and Actuators*, 20(1-2):123–133, November 1989.

[34] Stefan Johansson, Fredric Ericson, and Jan-Ake Schweitz. Influence of surface coatings on elasticity, residual stresses, and fracture properties of silicon microelements. *J. Appl. Phys.*, 65(1):122–128, January 1989.

[35] D. W. Hogg, J. G. Cohen, R. Blandford, S. D. J. Gwyn, F. D. A. Hartwick, B. Mobasher, P. Mazzei, M. Sawicki, H. Lin, H. K. C. Yee, A. J. Connolly, R. J. Brunner, I. Csabai, M. Dickinson, M. U. Subbarao, A. S. Szalay, A. Fernandez-Soto, K. M. Lanzetta, and A. Yahil. A blind test of photometric redshift prediction. *AJ*, 115:1418–1422, April 1998.

[36] D. C. Koo. Optical multicolors - a poor person's z machine for galaxies. *AJ*, 90:418–440, March 1985.

[37] R. J. Brunner, A. J. Connolly, A. S. Szalay, and M. A. Bershady. Toward more precise photometric redshifts: Calibration via CCD photometry. *ApJ*, 482:L21–+, June 1997.

[38] A. J. Connolly, A. S. Szalay, M. Dickinson, M. U. Subbarao, and R. J. Brunner. The evolution of the global star formation history as measured from the Hubble deep field. *ApJ*, 486:L11–+, September 1997.

[39] K. M. Lanzetta, A. Yahil, and A. Fernandez-Soto. Star-forming galaxies at very high redshifts. *Nature*, 381:759–763, 1996.

[40] E. Giallongo, S. D'Odorico, A. Fontana, S. Cristiani, E. Egami, E. Hu, and R. G. MCMahon. The photometric redshift distribution and evolutionary properties of galaxies up to $z \sim 4.5$ in the field of the quasar br 1202-0725. *AJ*, 115:2169–2183, June 1998.

[41] S. Arnouts, S. Cristiani, L. Moscardini, S. Matarrese, F. Lucchin, A. Fontana, and E. Giallongo. Measuring and modelling the redshift evolution of clustering: the Hubble Deep Field North. *MNRAS, astro-ph/9902290*, 1999.

[42] G. D. Coleman, C. C. Wu, and D. W. Weedman. Colors and magnitudes predicted for high redshift galaxies. *ApJS*, 43:393–416, July 1980.

[43] G. Bruzual A. and S. Charlot. Spectral evolution of stellar populations using isochrone synthesis. *ApJ*, 405:538–553, March 1993.

[44] M. A. Greenhouse. The NGST yardstick integrated science instrument module (ISIM) feasibility study. In *American Astronomical Society Meeting*, volume 194, pages 9113+, May 1999.

[45] M. Stiavelli. *private communication*, 1998.